Geophysical Journal International

Geophys. J. Int. (2020) **223,** 2148–2165
doi: 10.1093/gji/ggaa314
Advance Access publication 2020 September 23
GJI Seismology

Three-dimensional crustal *Vp* and *Vs* structures beneath the southern segment of the Tan-Lu fault revealed by active source and earthquake data

Yunpeng Zhang,[1] Baoshan Wang,[1,2,3] Tao Xu,[4,5] Wei Yang,[1] Weitao Wang,[1] Yihe Xu[1] and Lu Li[1]

[1] *Institute of Geophysics, China Earthquake Administration, Beijing,* 100081*, China. E-mail:* bwgeo@ustc.edu.cn
[2] *School of Earth and Space Sciences, University of Science and Technology of China, Hefei,* 230026*, China*
[3] *Mengcheng National Geophysical Observatory, University of Science and Technology of China, Hefei,* 230026*, China*
[4] *State Key Laboratory of Lithospheric Evolution, Institute of Geology and Geophysics, Chinese Academy of Sciences, Beijing,* 100029*, China*
[5] *CAS Center for Excellence in Tibetan Plateau Earth Sciences, Beijing,* 100029*, China*

Accepted 2020 June 16. Received 2020 June 14; in original form 2020 January 16

SUMMARY

The 2400-km-long Tan-Lu fault, the largest deformation zone in eastern China, plays a decisive role in the seismicity, regional tectonics and mineral deposits distributions. However, the velocity structure beneath the Tan-Lu fault, particularly in the southern segment, is poorly imaged due to the lack of local earthquakes. To obtain a high-resolution crustal structure image, we carried out an active source experiment by firing mobile airgun sources along the Yangtze River in the Anhui Province in October 2015. We manually picked 4118 *P* wave and 1906 *S* wave first arrival times from the airgun signals. We also collected 28 957 *P* wave and 26 257 *S* wave first arrival times from local earthquakes in a larger area. 3-D crustal velocity images beneath the southern segment of the Tan-Lu fault and surrounding areas are studied using traveltime tomography. Compared with the local earthquake data, the active source data provide better constraints on the upper crustal structure, which further refines the resolution of the lower-crust structure. The *Vp* and *Vs* crustal structures are consistent with the local geological settings, and earthquakes are primarily clustered near faults and are spatially correlated with low-velocity zones. Strong velocity contrasts are observed across the Tan-Lu fault zone, which is the main factor controlling local anomalies. The high *Vp*, *Vs* and *Vp*/*Vs* beneath the Qinling-Dabie orogenic belt and the Middle-Lower Yangtze River Metallogenic Belt may relate to Mesozoic lithospheric delamination and asthenospheric upwelling. These results also demonstrate that the mobile large-volume airgun sources are promising tools for 3-D crustal structure surveys.

Key words: Body waves; Airgun source; Seismic tomography; Crustal structure.

1 INTRODUCTION

The NNE-extending Tan-Lu (TanCheng-LuJiang) fault is the largest active deformation zone in eastern China (Deng *et al.* 2013; Wu *et al.* 2016). With a total length of 2400 km, it extends from Luobei County, Heilongjiang Province, to the southern end of Guangji County, Hubei Province. The formation mechanism and evolutionary history of the Tan-Lu fault are still under debate (Yin & Nie 1993; Xu & Zhu 1995; Wan *et al.* 1996; Zhu *et al.* 2004). Wan *et al.* (1996) proposed that the Tan-Lu fault initiated in the Middle and Late Triassic (230–208 Ma) due to the collisional orogeny between the North China block and South China block with 430 km of accumulated sinistral strike slip and gradually formed the current deep fault cutting down to the upper mantle. The Tan-Lu fault zone is also a linear gravity gradient belt, a regional magnetic anomaly transition boundary, and a well-known seismic zone (Wan *et al.* 2009; Wu *et al.* 2016), hosting several destructive historical earthquakes (e.g. the 1668 *M* 8.5 Tancheng earthquake and the 1975 *M* 7.3 Haicheng earthquake).

Email: bwgeo@ustc.edu.cn

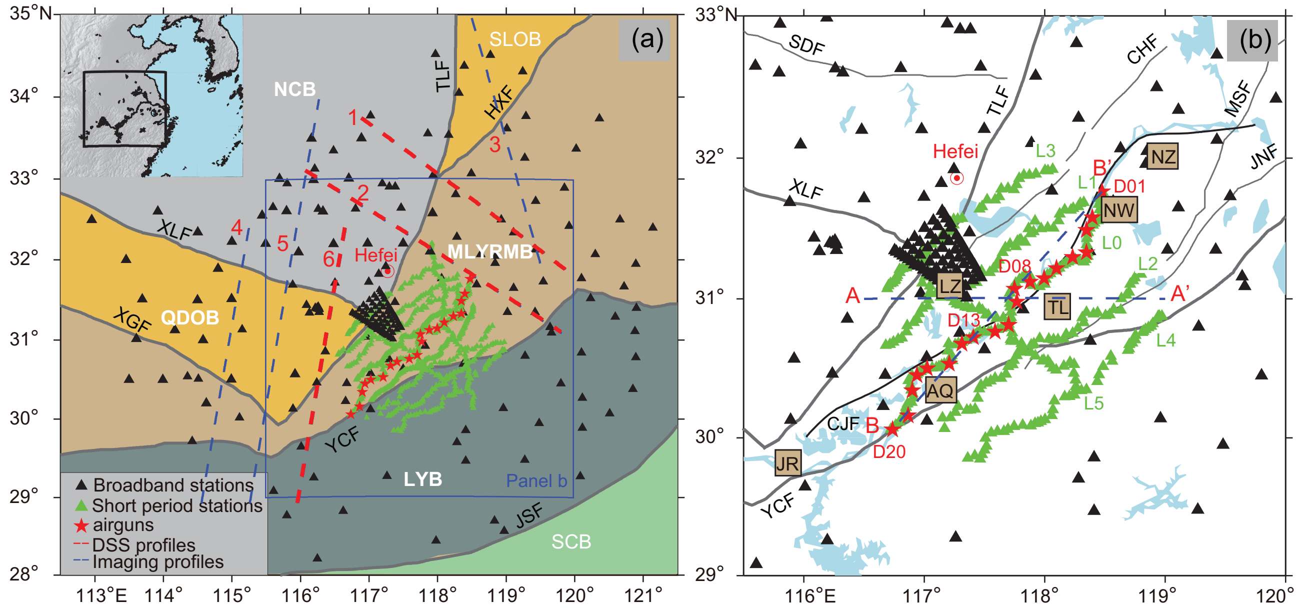

Figure 1. Map of the Anhui Airgun Experiment. The 20 red stars represent the fixed shooting sites (D01–D20). The black solid triangles indicate broad-band seismic stations, and the green triangles indicate short-period seismometers or geophones. The red and blue dashed lines indicate recent DSS profiles (Bai *et al.* 2016) and cross sections (see Section 5 for more details). The solid grey lines indicate geologic faults (Ouyang *et al.* 2015; Xu & Gao 2015; She *et al.* 2018). CHF, the Chuhe fault; CJF, the Changjiang fault; HXF, the Huaiyin-Xiangshui fault; JNF, the Jiangnan fault; JSF, the Jiangshan-Shaoxing fault; MSF, the Maoshan fault; SDF, the Shouxian-Dingyuan fault; TLF, the Tan-Lu fault; XGF, the Xiangfan-Guangji fault; XLF, the Xinyang-Lu'an fault; YCF, the Yangxin-Changzhou fault; LYB, the Lower Yangtze block; MLYRMB, Middle-Lower Yangtze River Metallogenic Belt; NCB, the North China block; QDOB, the Qinling-Dabie orogenic belt; SCB, the South China block; SLOB, the Sulu orogenic belt; AQ, Anqing; JR, Jiurui; LZ, Luzong; NW, Ningwu; NZ, Ningzhen; TL, Tongling. The abbreviation holds for the rest of this paper.

The Tan-Lu fault can be divided into three segments (northern, central and southern) by the Changtu (separates the northern and central segments) and Jiashan (segments the central and southern sections) counties according to different geological structures and seismicity (Luo *et al.* 2005; Wan *et al.* 2009; Deng *et al.* 2013; Wu *et al.* 2016). Currently, the seismicity along the fault is weak and inhomogeneous in the northern segment and the dominant mechanism is reverse for deep earthquakes and strike slip with thrust for shallow earthquakes (Ge *et al.* 2009). In the central segment, Quaternary strike-slip faulting is prevalent in the north (where strong historical earthquakes have occurred) but weakens in the portion south to the Suqian County (Shi *et al.* 2003). In the southern segment, the activity of strong earthquakes ($M > 5$) is rather weak although the small earthquakes are relatively active, and the focal fault rupture type is dip slip along the Tan-Lu fault but strike slip in the adjacent areas (Liu *et al.* 2006).

Recently, the southern segment of the Tan-Lu fault and its adjacent regions (Fig. 1) have become the focus of seismological, tectonic, and geological studies. This area is a tectonic syntaxis of the Qinling-Dabie orogenic belt, North China block and Yangtze block. The southern segment of the Tan-Lu fault intersects with the Xiangfan-Guangji fault; however, the southward extension of the Tan-Lu fault is still under debate (Yao & Fang 1981; Xu *et al.* 2001). The Qinling-Dabie orogenic belt is located to the west of the Tan-Lu fault, which contains widespread ultrahigh-pressure (UHP) rocks, resulting from the collision of the Yangtze and Sino-Korean cratons in the Mesozoic (Wang *et al.* 2000). However, the depth extension of the UHP rocks is yet to be determined (Wang *et al.* 2000; Xu *et al.* 2000; Li *et al.* 2002; Ding *et al.* 2017). In addition, this area is rich in metallic and polymetallic deposits (Dong *et al.* 2010). Most deposits are clustered along the Yangtze River (e.g. Ningzhen, Ningwu, Luzong, Tongling, Anqing, Guichi and Jiurui) and in adjacent regions (Jiang *et al.* 2013). However, their extension, characteristics and formation mechanisms are debatable (Li 2001; Lyu *et al.* 2003, 2005; Hou *et al.* 2007; Ling *et al.* 2009; Li *et al.* 2013). High-resolution crustal imaging may provide some evidences to resolve these controversies.

Over the past few decades, numerous imaging attempts have been made around the southern segment of the Tan-Lu fault using the deep seismic sounding (DSS, Bai *et al.* 2016), which provide important insights into the understanding of fine structures. Recently, 3-D *S*-wave velocity structures also have been obtained from ambient noise tomography (Luo *et al.* 2012; Ouyang *et al.* 2015; Meng *et al.* 2019). However, these previous geophysical studies have focused on individual profiles or specific small areas. Further, *P*- and *S*-wave images were obtained separately in previous studies, which may impede the understanding of underground structures (Ryberg *et al.* 2012; Zhang *et al.* 2014). Therefore, large-scale 3-D *Vp* and *Vs* structures of this region are still in demand to further investigate regional geologic features, seismogenic mechanisms, mineral resource distributions and local seismic hazard assessment (Zhang *et al.* 2005; Yao *et al.* 2014; Wu *et al.* 2016).

Local and teleseismic earthquake body-wave tomography can provide *Vp* and *Vs* velocity images synchronously (e.g. Zhao *et al.* 1992). However, the seismicity in this region was uneven (strong in the west while weak along the Yangtze River), which may affect the imaging results. High performance active sources, to some extent, can fill the gaps of natural earthquakes. The use of conventional active sources (e.g.

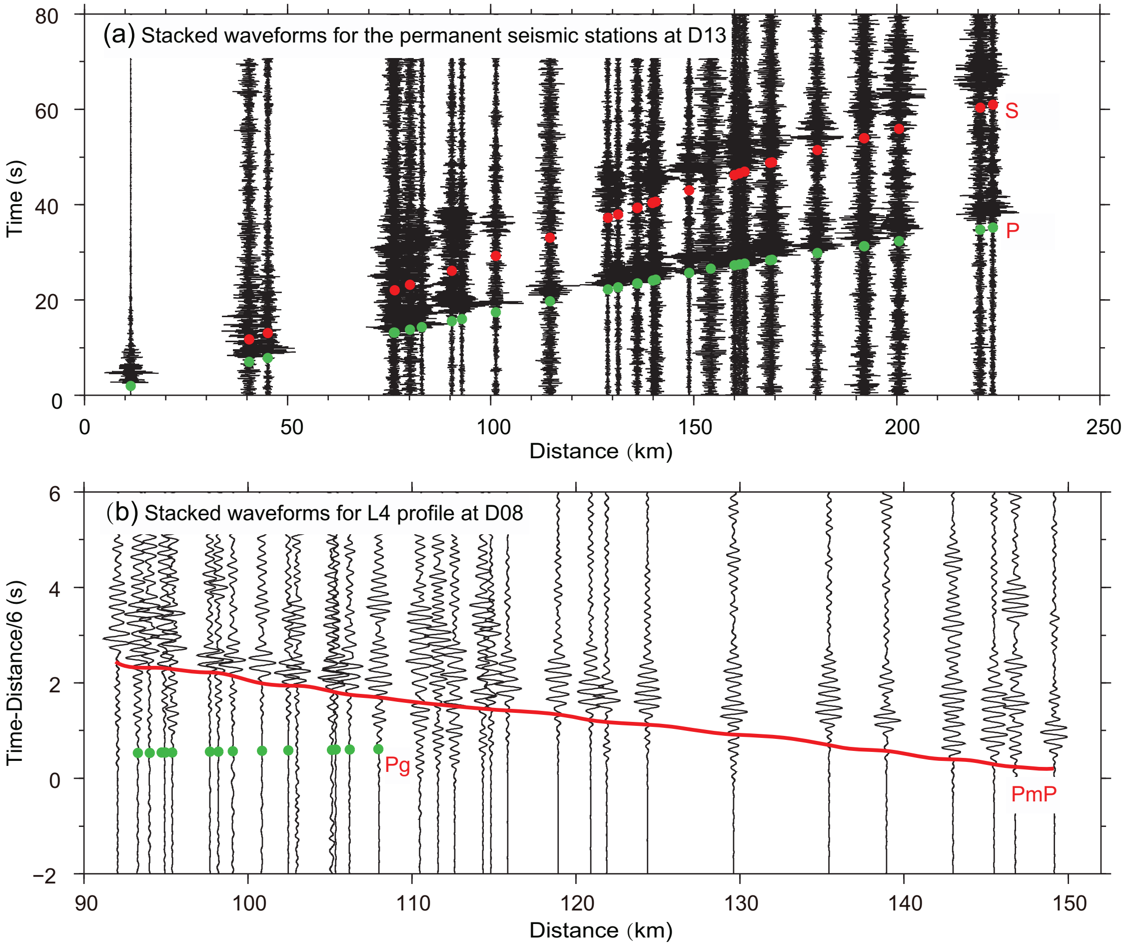

Figure 2. The linearly stacked waveforms using the RMS data selection strategy for the permanent seismic stations at D13 (a) and for L4 profile at the D08 (b). The green and red dots indicate the first arrival *P* and *S* phases, respectively. The waveforms with a bandpass filter of 2–8 Hz are plotted, which is the dominant frequency (Wang *et al.* 2018).

explosives) has been more restricted due to environment and safety issues. Recently, the large-volume airguns are proposed to excite seismic waves in the on-shore water bodies (Chen *et al.* 2017; Wang *et al.* 2018, 2020).

Airgun sources have long been used in exploring structures in marine areas (Vaage *et al.* 1983), near-shore areas (Godfrey *et al.* 2002; Qiu *et al.* 2007; Cai *et al.* 2015; Guo *et al.* 2019), and volcanic areas (Zollo *et al.* 2003; Evangelidis *et al.* 2004; Calvert *et al.* 2008; Zandomeneghi *et al.* 2009; Shalev *et al.* 2010; García-Yeguas *et al.* 2012; Paulatto *et al.* 2012). Using small airguns, Hao *et al.* (2013) also imaged the detailed shallow fault structures along the Mississippi River. Herein, to study the 3-D high-precision velocity structures beneath the southern segment of the Tan-Lu fault, we performed an active source survey in this region (referred to as the Anhui Airgun Experiment hereafter), which, to our best knowledge, is the first on-shore 3-D crustal structure exploring experiment using airgun source.

The records from the Anhui Airgun Experiment have been used to image the *P*-wave (Tian *et al.* 2018) and *S*-wave (She *et al.* 2018) velocity structures of the upper crust based on the first arrival *P* wave and surface wave data, respectively. Further, airgun sources can radiate strong *S* waves associated with the *P*-wave energy (Wang *et al.* 2018, 2020). In this paper, we perform body-wave tomography of the southern segment of the Tan-Lu fault and adjacent area using both *P*- and *S*-wave data from the airgun sources. We also compare imaging resolution to the result of local earthquakes tomography and perform a combined inversion to obtain high-resolution results.

2 THE ANHUI AIRGUN EXPERIMENT

2.1 Setting of the Anhui Airgun Experiment

During the period of 10–20 October 2015, we performed an active source experiment by firing mobile airgun sources along the Yangtze River in the Anhui Province, eastern China. The airgun source was composed of four individual guns with total volume of 8000 in^3 mounted on the R/V Yanping II. In total, 4845 airgun shots were fired along the 300-km-long Ma'anshan-Anqing segment of the Yangtze River (Fig. 1). Of the 4845 shots, 2973 shots were fired at 20 fixed shooting sites (45–339 shots at each site) and 1872 shots were fired in the walkway (Xu *et al.* 2016). The receiving system was composed of 109 permanent three-component broad-band seismic stations (Data Management Centre

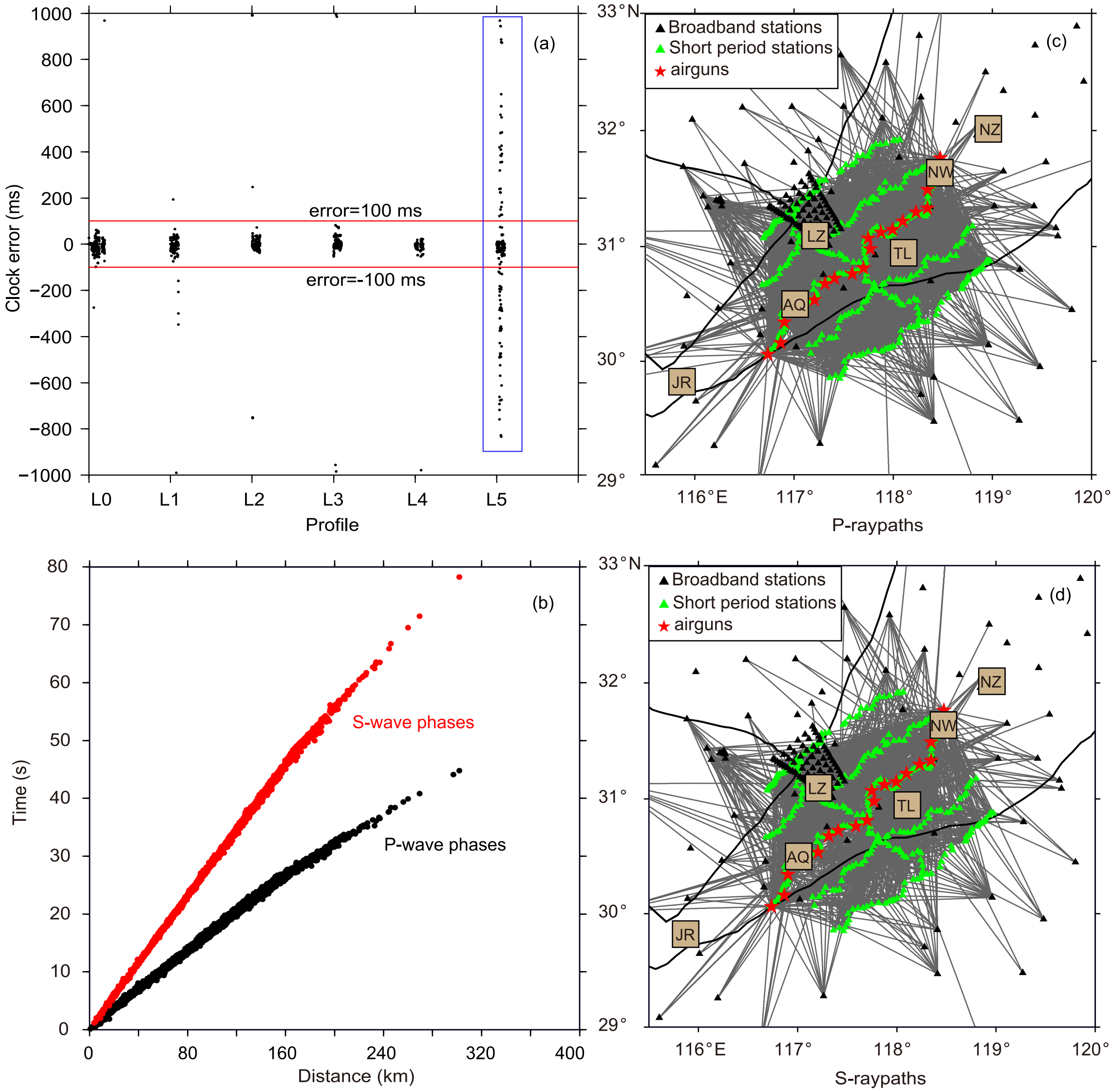

Figure 3. (a) Clock error distribution of the L0–L5 profile stations. (b) Manually picked traveltimes of the first arrival *P* and *S* phases. Panels (c) and (d) are the ray coverage of the *P* waves and the *S* waves, respectively.

of China National Seismic Network 2007; Zheng *et al.* 2010) and 853 portable three-component short-period seismometers or geophones (Fig. 1). The portable stations were deployed along 11 profiles (nine parallel and two perpendicular to the source trace). Seismographs were deployed with an average spacing of 2 km in the riverside profile (L0) and 4–5 km in the other profiles. Unfortunately, due to instrumental problems, only 6 of the 11 profiles recorded the airgun signals (Fig. 1b). Both sources and seismometers were synchronized to the global positioning system.

2.2 Arrival time picking

We first cut the three-component airgun records of each shot 10 s before and 200 s after the origin time. The signals from the 20 fixed position shots were then stacked to enhance the signal-to-noise ratio (SNR). The records from the walkway shots were not used herein. The linearly stacked waveforms (Fig. 2) obtained using the root-mean-square (RMS) data selection strategy (Jiang *et al.* 2017) have higher SNRs compared with linear stacking (Zhang *et al.* 2016; Tian *et al.* 2018).

Then, we manually picked the first arrival *P* and *S* phases from the stacked waveforms. Stations with average clock errors >100 ms were discarded (Fig. 3a). Eventually, we obtained 4118 *P*-wave first arrival times. Exploiting the high shear wave energy from the airguns (Chen *et al.* 2017; Wang *et al.* 2018), we also picked 1906 *S*-wave first arrival times. Both the *P*- and *S*-wave ray paths cover the study area fairly well (Fig. 3).

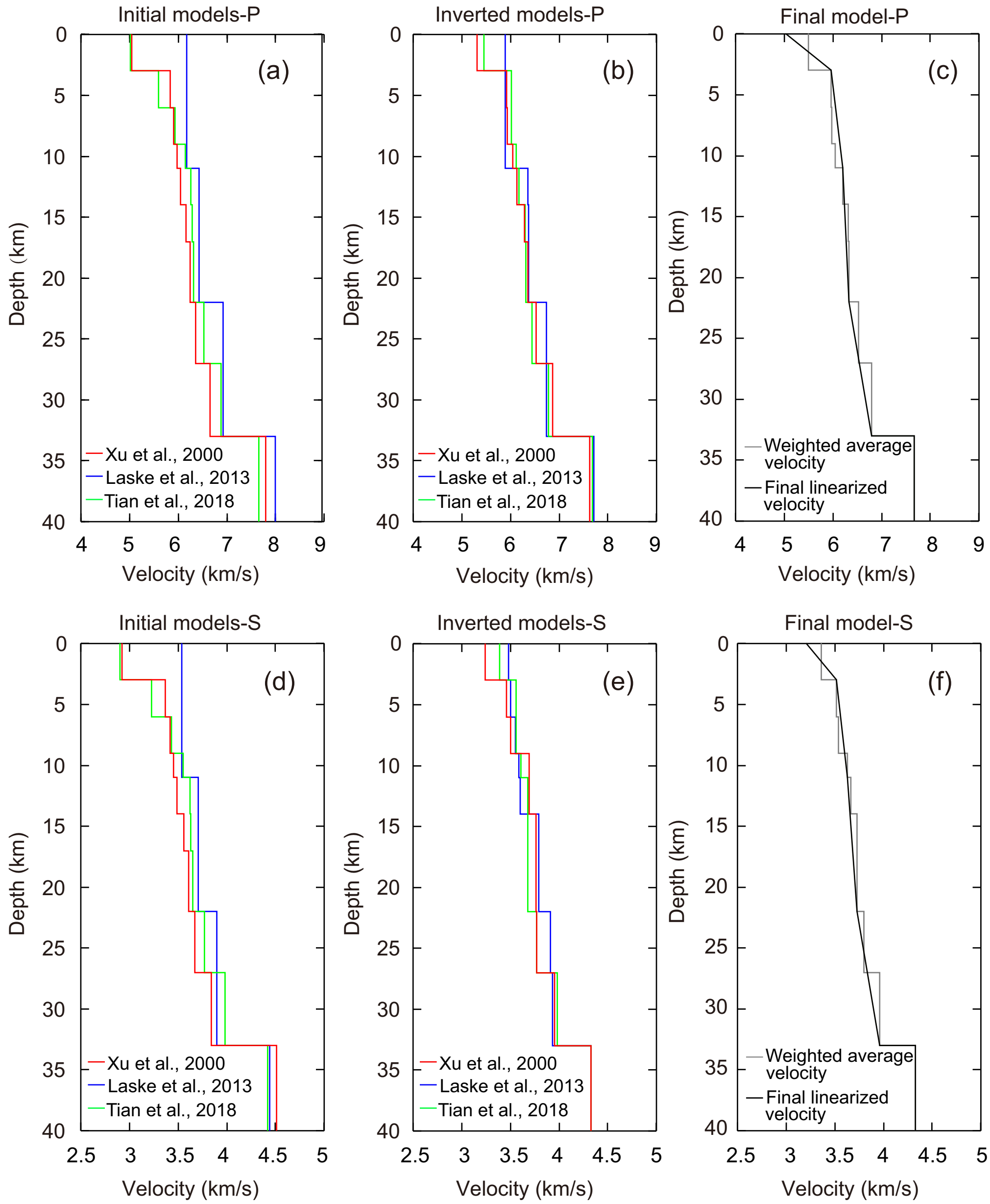

Figure 4. (a) Three 1-D *P*-wave velocity models averaged from the initial models (Xu *et al.* 2000; Laske *et al.* 2013; Tian *et al.* 2018). (b) The inverted models obtained from the VELEST program starting from each of the different initial models shown in panel (a). (c) The weighted average velocity and the final 1-D *P*-wave velocity model ($V_{P\mathrm{model}}$). Panels (d)–(f) correspond to the *S*-wave models, and the 1-D *S*-wave velocity initial models in panel (d) were divided by 1.73 compared to the *P*-wave velocities in panel (a).

3 1-D VELOCITY MODEL FROM AIRGUN DATA

A good initial 1-D velocity model is of key importance in local earthquake tomography which is generally a nonlinear inversion process (Crosson 1976; Thurber 1983; Kissling 1995; Matrullo *et al.* 2013). To obtain appropriate 1-D *P*- and *S*-wave velocity models for our study region (28°–34°N, 114°–120°E), we used the VELEST package (Kissling *et al.* 1994). The VELEST package can estimate the 1-D (layered) velocity models with station corrections via an inversion of the damped least-square matrix of the traveltime partial derivatives (Kissling 1995). First, the average depths of the upper-middle crust, the middle-lower crust and the Moho discontinuities were estimated from crust1.0 (Laske *et al.* 2013) as 10.98, 21.88 and 32.84 km, respectively. The average Moho depth is consistent with that estimated from the receiver functions [32.45 km by Li *et al.* (2014) and 32.70 by He *et al.* (2014)].

We then jointly inverted the *P*- and *S*-wave velocity models with different initial models (Xu *et al.* 2000; Laske *et al.* 2013; Tian *et al.* 2018) using airgun data and set the layers with depth of 3-, 6-, 9-, 11-, 14-, 17-, 22-, 27- and 33-km after testing different thicknesses. We did not add a low-velocity layer to avoid potential instabilities in the inversion (Kissling 1995). For each initial model, a stable solution was obtained after 3–15 iterations. To make the initial model more precise, we first average of the three inverted models with weighting factors 0.3, 0.2 and 0.5 for Xu *et al.* (2000), Laske *et al.* (2013) and Tian *et al.* (2018), respectively. We then linearized this result by considering the

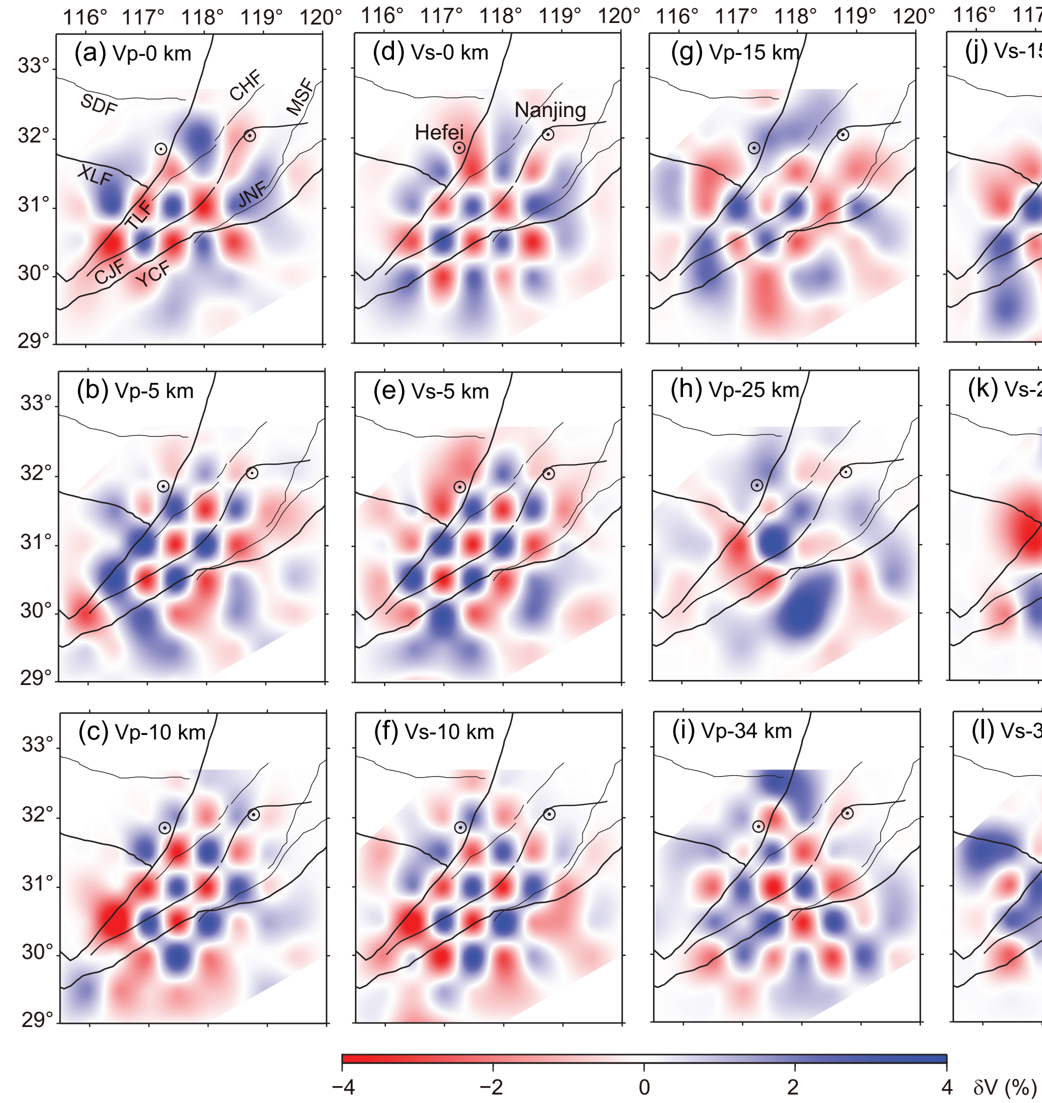

Figure 5. Result of checkerboard resolution test for *P*- and *S*-wave velocity at different depths inverted using the airgun data.

values at 3, 11, 22 and 33 km as the final 1-D *P*- and *S*- wave velocity models ($V_{P\mathrm{model}}$ and $V_{S\mathrm{model}}$, respectively). The details of the inversion process are displayed in Fig. 4.

The velocities <20 km in inverted models are better converged than those in the initial models (Figs 4a and b). And our data have good ray path coverage only for depths <20 km (Fig. 5). The velocity of the uppermost mantle is ~7.67 km s^{-1}, which coincides with the result from Pn tomography (Gu *et al.* 2016).

4 BODY-WAVE TRAVELTIME TOMOGRAPHY

4.1 Tomography using airgun data

Using the precise active source locations, the manually picked traveltimes, and the final 1-D *P*- and *S*-wave velocity models (Fig. 4), we only inverted the velocity structure without source relocation when we implemented body-wave traveltime tomography using the TOMOG3D program (Zhao *et al*. 1992, 1994). The gridding setting of the tomographic inversion was selected according to the checkerboard test (Zhao *et al*. 1992, 1994). For the checkerboard tests, we alternately added ±4 per cent perturbations to the adjacent gridpoints. In addition, random errors with a normal distribution and a standard deviation of 0.1 s were added to the theoretical traveltimes to simulate the noise effect. According to the ray coverage and the checkerboard test, we set the grid spacing to 0.5° × 0.5° horizontally and 0, 5, 10, 15, 25 and 34 km in depth. The checkerboard results indicate that the velocity images of the upper crust and uppermost mantle are well resolved, whereas the middle- and lower-crust images are poorly constrained (Fig. 5).

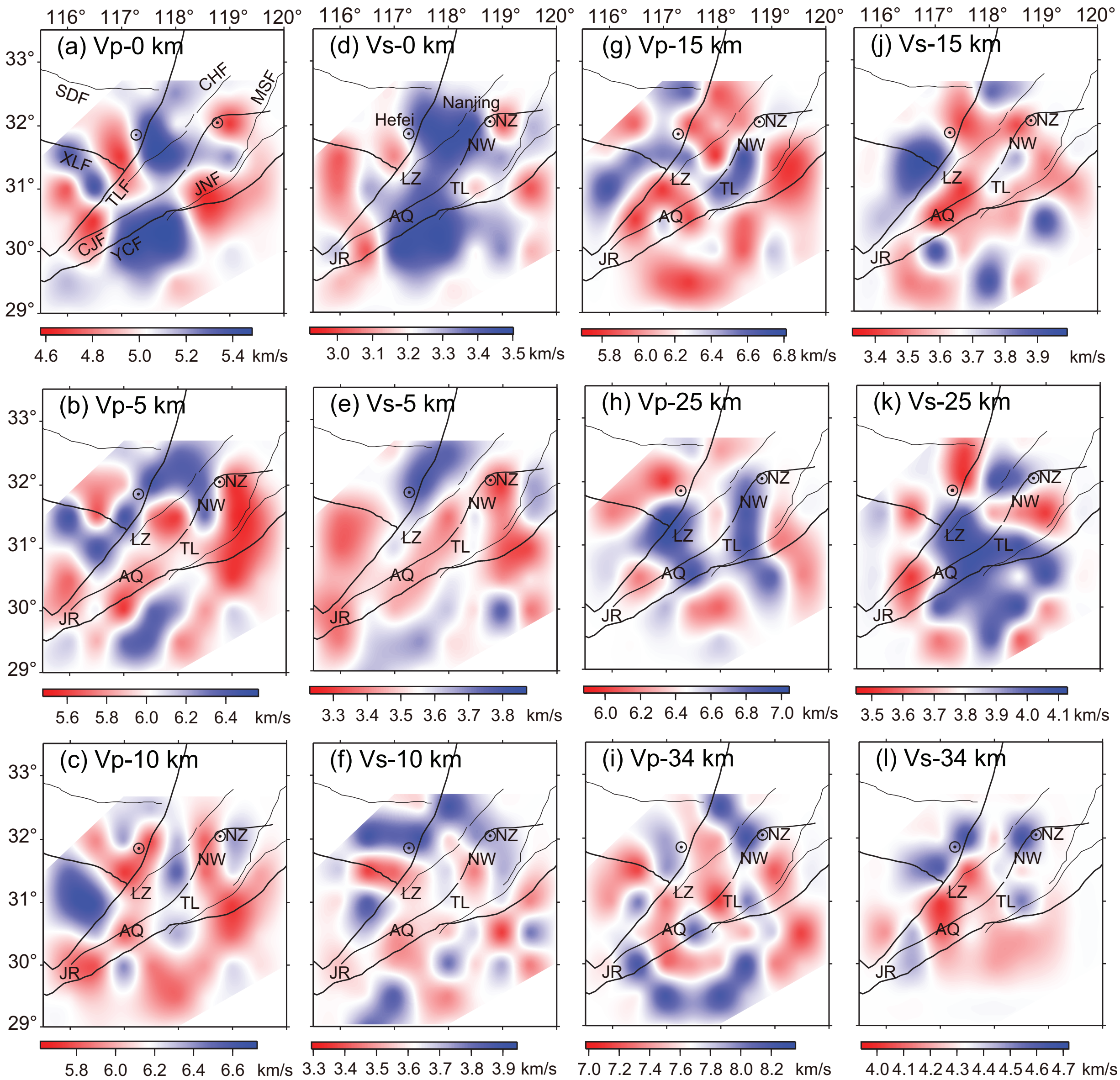

Figure 6. *P*- and *S*-wave velocity images at different depths inverted using the airgun data.

In the tomography, we only used the data with traveltime residuals (absolute difference between the observed and calculated traveltimes) ≤2 s for both the *P* and *S* waves. In addition, only grids nodes with hit counts ≥10 were used in the inversion. After various tests, the damping factor was set to 3 according to the tradeoff curve (Eberhart-Phillips 1986; Aster *et al.* 2013).

In general, images at depths of 0, 5, 10, 15 and 34 km are very reliable (Fig. 5). Our 3-D model (Fig. 6) is consistent overall with the geological settings. For both *P*- and *S*-wave images, the Qinling-Dabie orogenic belt presents high-velocity anomalies whereas the Middle-Lower Yangtze River Metallogenic Belt is widespread of low-velocity anomalies (Fig. 6). Meanwhile, clear velocity contrasts are observed crossing major fault zones (e.g. the Tan-Lu and Chuhe faults).

4.2 Tomography using both airgun and earthquake data

The airgun data cover only part of our study area, and the checkerboard results indicate that the resolving ability of the airgun data is poor in the middle and lower crust (Fig. 5). To get better crustal images, we added local earthquakes to cover a larger area and to better resolve the velocity structure of the middle to lower crust. We used 3560 local earthquakes with magnitudes >1 from January 2008 to March 2018 (China Earthquake Network Center, CENC bulletin), these earthquakes have location uncertainties less than 5 km (accuracy of class 1 in CENC bulletin). The 10-years earthquake data cover the study area fairly well, leaving a small gap in the Middle-Lower Yangtze River Metallogenic Belt, the gap is partially filled by the airgun data (Fig. 7).

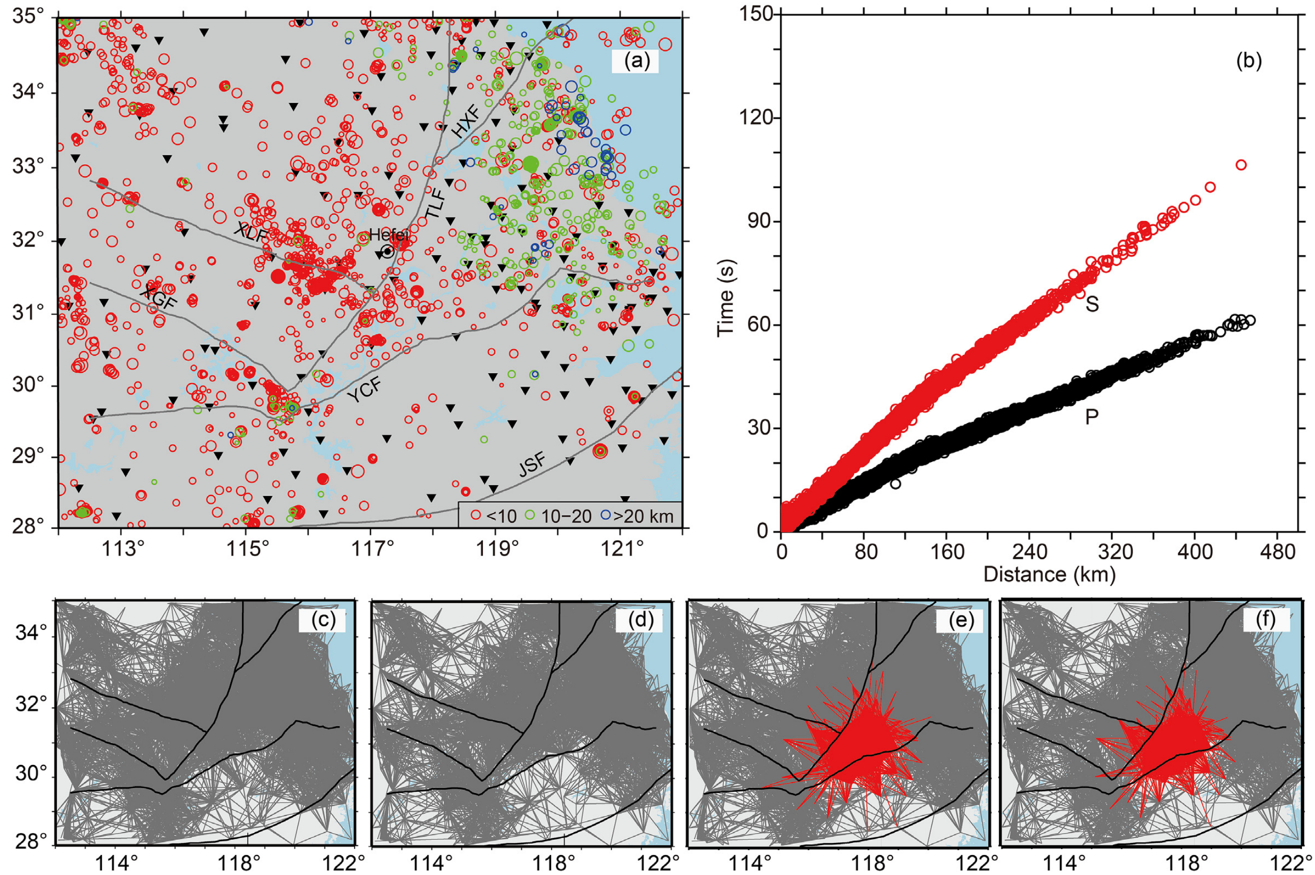

Figure 7. (a) The distribution of local earthquakes ($M > 1$). (b) Traveltime curve of the local earthquakes after deleting data with residual errors >2 s (28 957 *P* phases and 26 257 *S* phases). Panels (c) and (d) are *P*- and *S*-wave ray coverage of the local earthquakes, respectively. Panels (e) and (f) are the combined *P*- and *S*-wave ray coverage of the airgun sources (red lines) and the local earthquakes (grey lines), respectively.

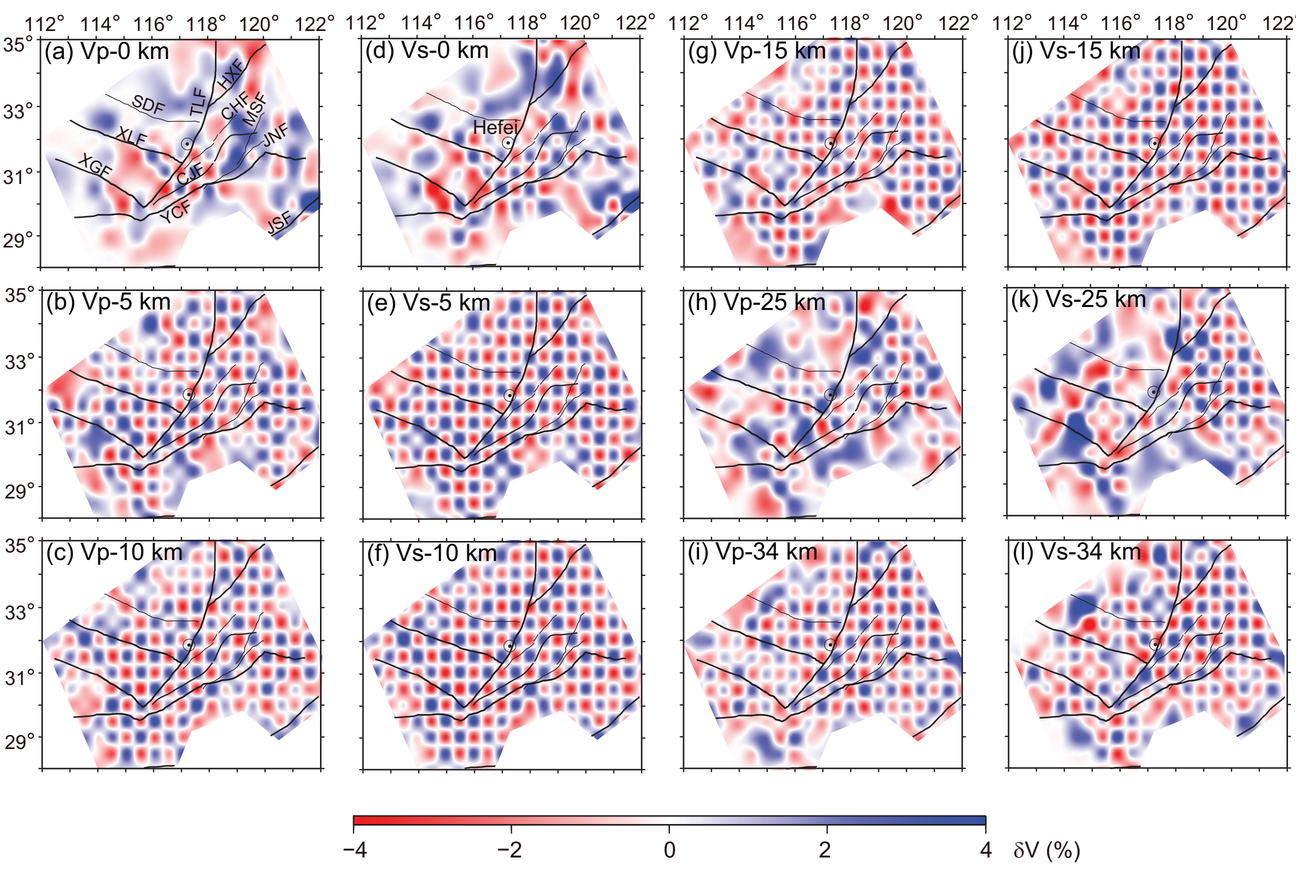

Figure 8. Result of checkerboard resolution test for *P*- and *S*-wave velocity at different depths using the airgun sources and local earthquakes.

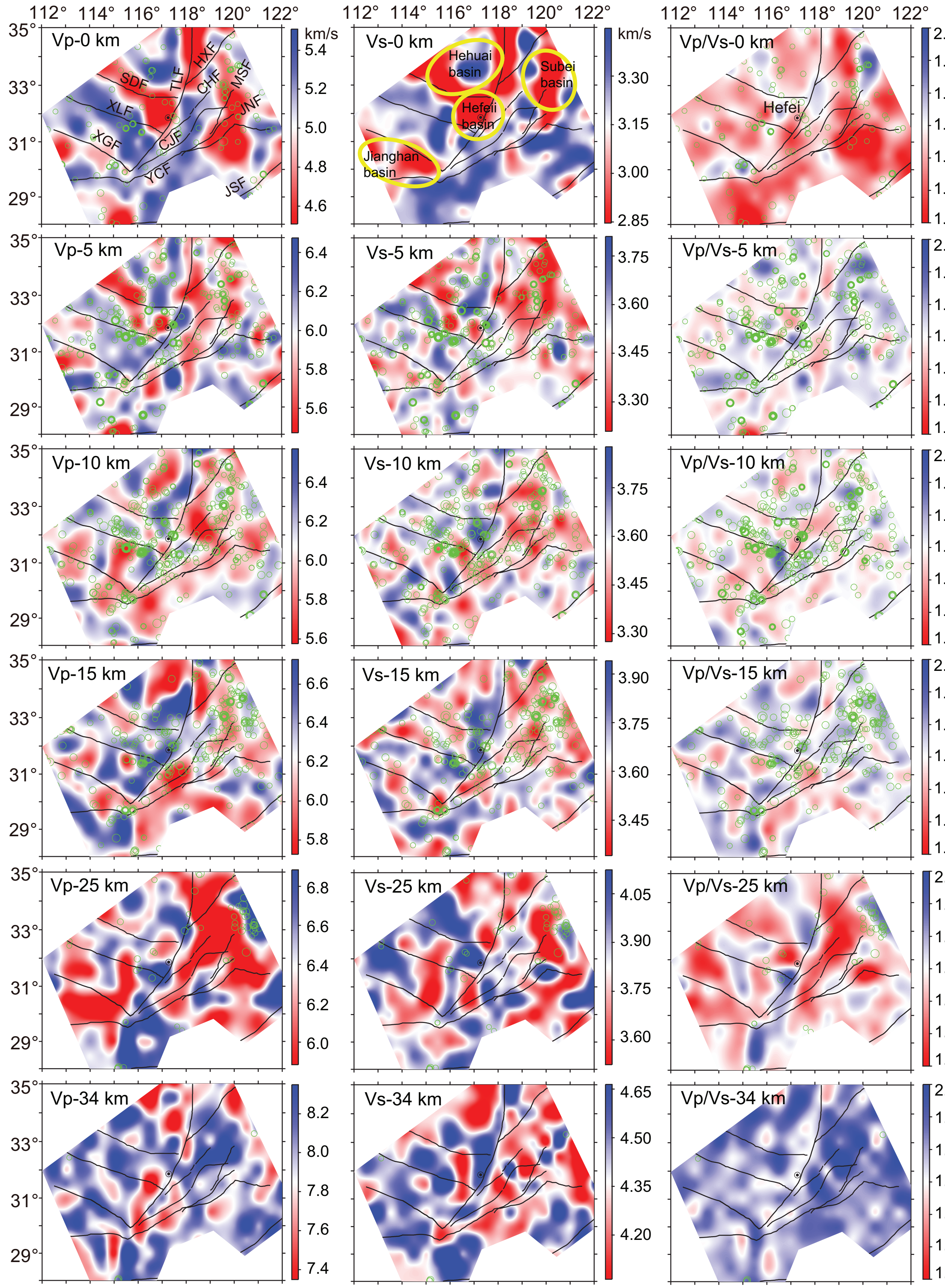

Figure 9. Inverted *P*-wave, *S*-wave velocity images and *Vp*/*Vs* model at different depths using the airgun sources and local earthquakes. The green circles indicate local earthquakes with magnitudes >2 (within 5 km above and below the drawing depth).

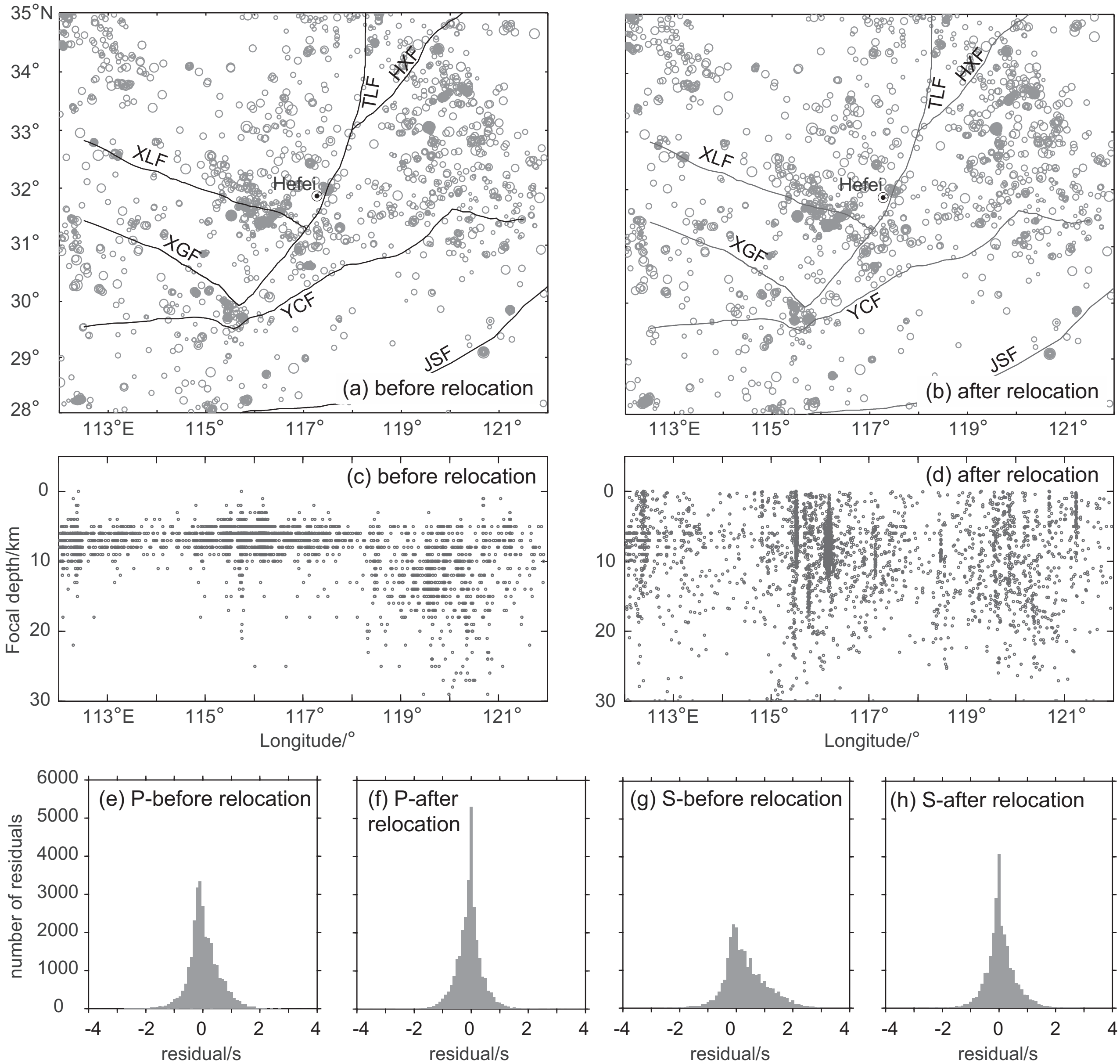

Figure 10. The earthquake ($M > 1$) distribution and traveltime residuals before and after earthquake relocation.

Through the same tests, we used the same inversion parameters as in the airgun source tomography (Section 4.1) and obtained the result of checkerboard resolution test and the velocity images at different depths using both airgun sources and the local earthquakes (Figs 8 and 9). After adding the earthquakes, the middle and lower crust imagings are better constrained (Fig. 8).

After the inversion, the distribution of the earthquake location and traveltime residuals are improved (Fig. 10). Uncertainties of the hypocentral location are 0.01° and 2.92 km in the horizontal and depth directions after inversion (Figs 10b and d). In addition, the traveltime residuals after inversion are remarkably reduced (Figs 10e and g), and follow a Gaussian distribution centred at 0 s for both *P* and *S* wave (Figs 10f and h).

5 DISCUSSION

5.1 Resolving abilities of the airgun sources and earthquakes

Results of checkerboard tests indicate that the airgun sources and local earthquakes have different resolving abilities for the crustal structure. To further investigate this difference, we cut a vertical cross section along the latitude of 31°N (AA′ in Fig. 1b) from both the checkerboard and real data tomography (Fig. 11).

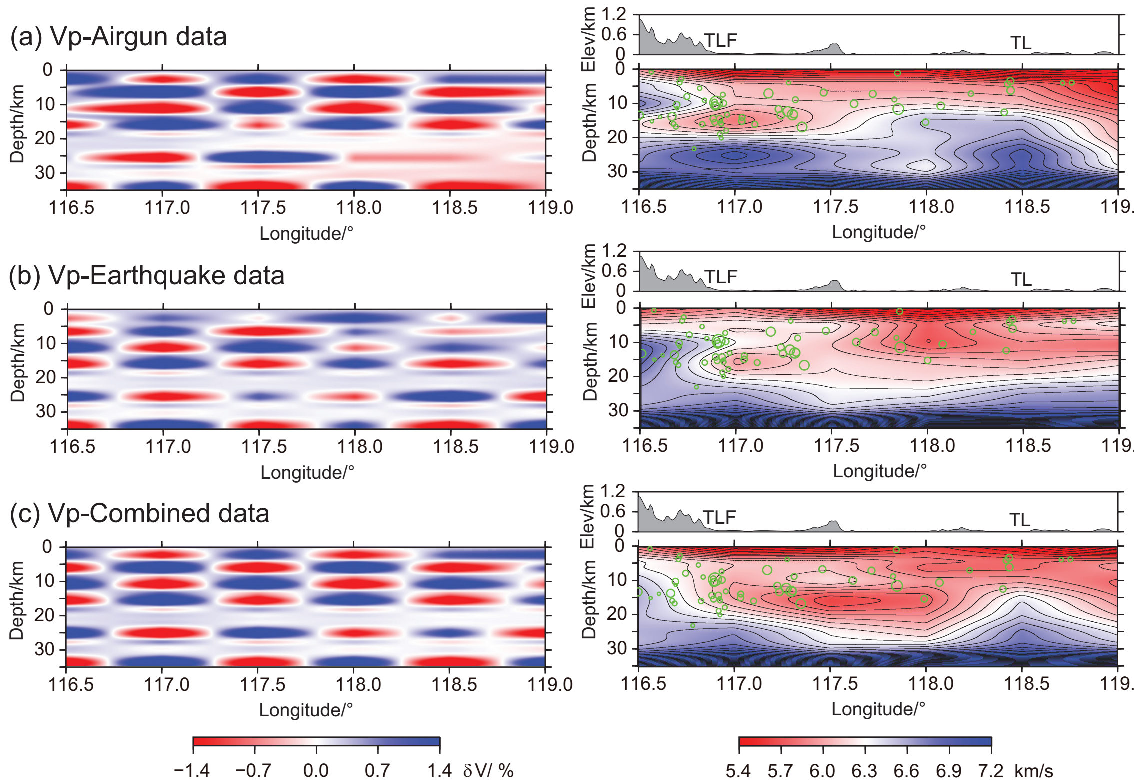

Figure 11. Result of checkerboard resolution test and velocity image for *P*-wave velocity of the vertical section along the latitude of 31°N (profile AA′ in Fig. 1b). The thin green circles indicate local earthquakes within 0.25° on both sides of the profile, and this also holds for the rest of this paper.

As suggested in Sections 4.1 and 4.2, the airgun sources resolve the upper crust better than the lower crust, whereas the earthquake data pose more constraints on the lower crust. Notably, both the upper and lower crusts are better resolved by the combined data than by the airgun or earthquake data alone (Fig. 11). A better constraint in one location may decrease ambiguities in other parts, which is also the situation in joint tomography using different geophysical data (e.g. Zhang *et al.* 2014; Syracuse *et al.* 2017). The velocity images (Fig. 11c) resolved with the combined data resemble the structures obtained from the airgun data tomography (Fig. 11a) in the upper crust and earthquake data tomography (Fig. 11b) in the lower crust.

Besides the first arrival *P* and *S* waves, the stacked waveforms of the airgun data have abundant PmP phases (Fig. 2b), which can also be used to improve the resolution of the lower crust (e.g. Zhao *et al.* 2005). In the future study, we will refine the tomography by adding more phases.

5.2 Main features of the velocity anomalies and correlations with the earthquake distribution

For our velocity images, in the shallow part (0 and 5 km), the Qinling-Dabie orogenic belt presents a high-velocity anomaly, whereas the Hehuai, Jianghan, Hefei and Subei basins (Fig. 9) show low-velocity anomalies. These anomalies are consistent with the geological settings and in agreement with the results reported by Xu *et al.* (2001), Ouyang *et al.* (2015) and Meng *et al.* (2019).

The most significant characteristic in our imaging result is the velocity variations along the NNE direction, this pattern is in corresponding with the extension of the Tan-Lu fault. Distinct whole crust velocity differences exist between two sides of the Tan-Lu fault, which implies that the Tan-Lu fault is the main factor controlling these anomalies and is a deep fault cutting down to the Moho discontinuity (Xu *et al.* 2001; Huang *et al.* 2011; Ding *et al.* 2017). The receiver function result (Shi *et al.* 2013) also revealed the uplifted Moho (even the LAB, lithosphere–asthenosphere boundary) beneath the Tan-Lu fault.

In an example of a profile (Fuliji-Fengxian) across the Tan-Lu fault (Fig. 12), there is an obvious slant high–low-velocity boundary beneath the Tan-Lu fault, with higher velocities in the North China block. Meanwhile, the Subei basin shows low velocities in the upper crust for both the *P*- and *S*-wave velocity structures. These features are similar to the results reported by Bai & Wang (2006). Moreover, our result implies that the Tan-Lu fault cuts down to the Moho (not only for the upper and middle crust), which is consistent with the results reported by Zheng & Teng (1989), Weng *et al.* (1990) and another profile along Lingbi-Siyang (∼80 km north of profile 1, Liu *et al.* 2015). Liu *et al.* (2015) also revealed that the transition of the crust–mantle transition zone beneath the Tan-Lu fault is obviously uplifted, corresponding to the lower crust high-velocity anomaly in our model, which may be an upwelling channel for hot material from the upper mantle.

After relocation, the earthquakes primarily concentrate near faults such as the Xiangfan-Guangji and Xinyang-Lu'an faults (Figs 9 and 10). Meanwhile, local earthquakes are primarily distributed in the low-velocity zone of the northeast region. In general, for a low-velocity

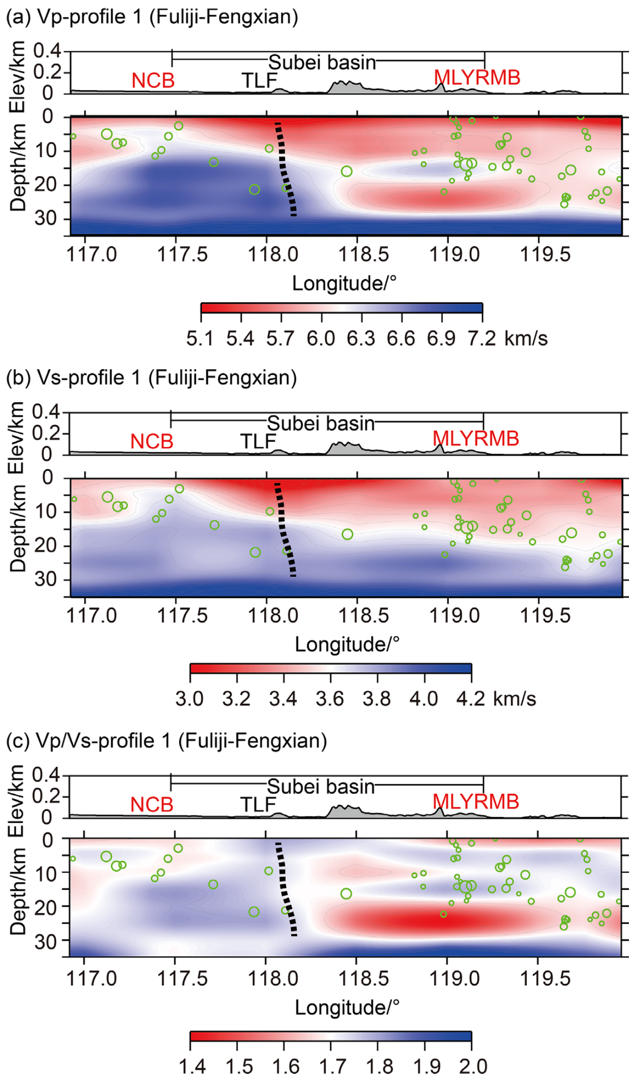

Figure 12. The *P*-wave, *S*-wave velocity images and *Vp*/*Vs* model for the combined inversion of the active sources and local earthquakes of the Fuliji-Fengxian profile (profile 1 in Fig. 1a). The black lines are the predicted dip of Tan-Lu fault.

layer within the crust (in a weakened crust), deformation occurs via viscous or dislocation creep in response to regional plate stress and via elastic failure in small earthquakes (Long & Zelt 1991; Huang *et al.* 2011).

5.3 Crustal structures of the Qinling-Dabie and Sulu orogenic zones

To better understand the crustal structures, the thickness and occurrence of UHP rocks beneath the Qinling-Dabie and Sulu orogenic belts, we prepared vertical sections beneath four profiles (profiles 3–6 in Fig. 1a) in Fig. 13.

Beneath the Qinling-Dabie orogenic belt, three profiles present *P*- and *S*-wave velocities higher than the surrounding areas. The *Vs* in profile 6 (Fig. 13c) shows the same high-low velocity trend with the nearby profile CC′ in Meng *et al.* (2019). Meng *et al.* (2019) explained the high-velocity anomaly beneath the Qinling-Dabie orogenic belt related to the lithosphere and lower crust delamination and Mesozoic volcanic magmatism in eastern China. Furthermore, the *Vp* in profile 6 (Fig. 13c) is similar to the results reported by Wang *et al.* (2000) and the red dashed line indicates the suture (dipping north) between the Sino-Korean and Yangtze cratons. However, the high-velocity anomaly in our result extends to the middle and lower crust, which is deeper than the anomaly revealed by Wang *et al.* (2000).

The *Vp*, *Vs* and *Vp*/*Vs* images beneath the Sulu orogenic belt (Figs 13d) indicate there are velocity contrasts across the Huaiyin-Xiangshui and Tan-Lu faults, with the velocity increasing from south to north in different blocks. Furthermore, the low-velocity zone of the upper crust disappears after entering the Sulu UHP metamorphic belt. These features are the same as those reported by Meng *et al.* (2019) via ambient noise tomography. They postulated that the low-velocity anomalies at depths of 10 km may be a fracture zone between the UHP metamorphic rock and the Yangtze block, which may be the boundary between the Yangtze and North China blocks (black dashed line in Fig. 13d).

For these profiles, high-velocity (and high *Vp*/*Vs*) zones at depths of 5–10 km (green circles in Fig. 13) may correspond to HUP rocks, consistent with the results reported by Wang *et al.* (2000), Yang (2002), Huang *et al.* (2011) and Luo *et al.* (2012). Moreover, high-velocity

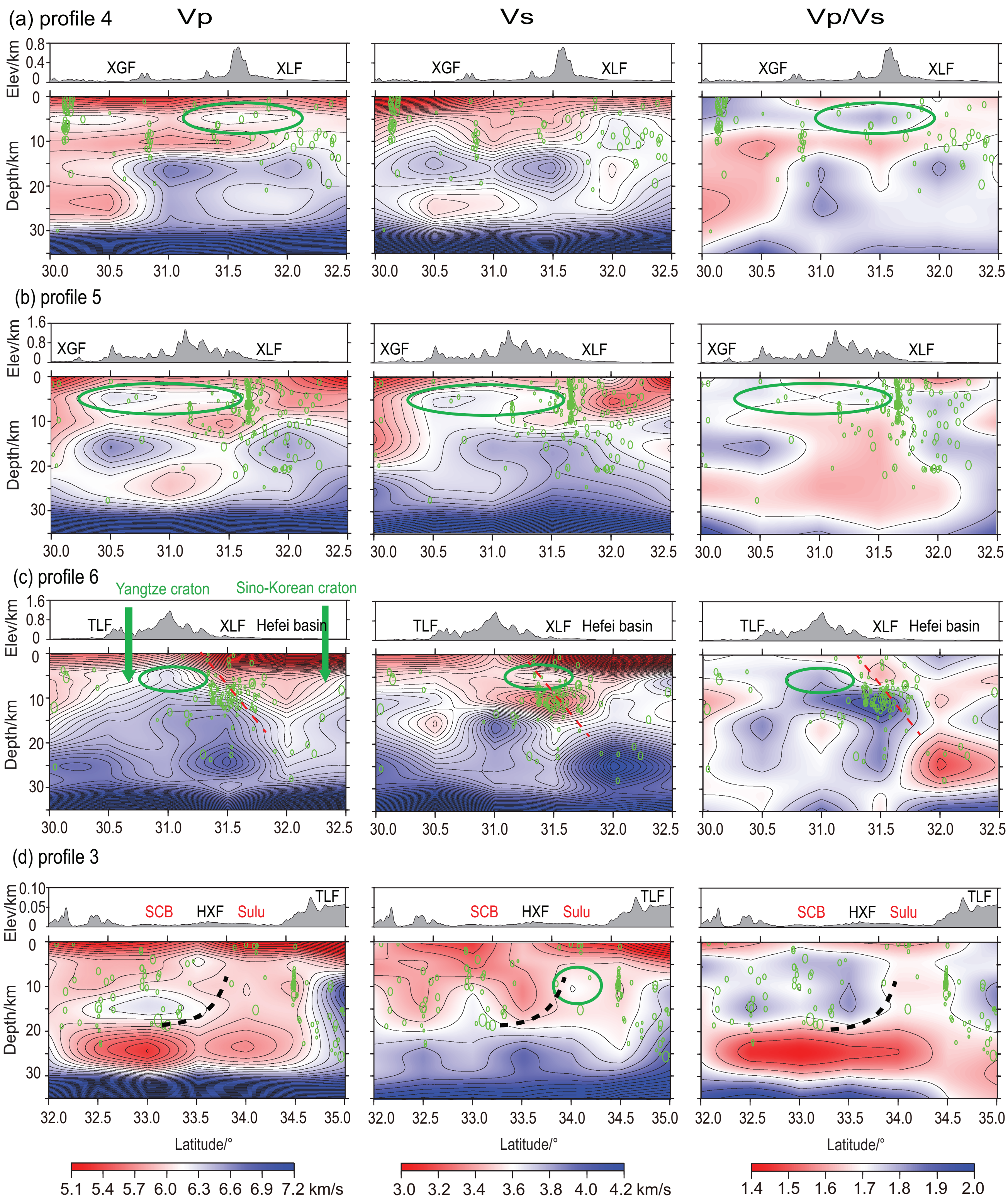

Figure 13. Vertical depth section of the *P*-wave, *S*-wave velocity images and *Vp*/*Vs* models beneath the Qinling-Dabie and Sulu orogenic belts from the combined inversion of the active sources and the local earthquakes: (a) profile 4 in Fig. 1; (b) profile 5 in Fig. 1; (c) profile 6 in Fig. 1 and (d) profile 3 in Fig. 1.

anomalies are generally distributed in the middle crust (at depths of 11–22 km), as reported by Luo *et al.* (2012) and Meng *et al.* (2019). These high-velocity anomalies in the middle crust may be related to lithospheric delamination and asthenospheric upwelling. In such a case, magma originates from the partial melting of the middle and lower crust, then enters the overlying crust through intrusions, and directly cools in the upper and middle crust to form high-velocity anomalies (Zhao & Zheng 2009; Liu *et al.* 2016; Meng *et al.* 2019). Xu *et al.* (2001) even

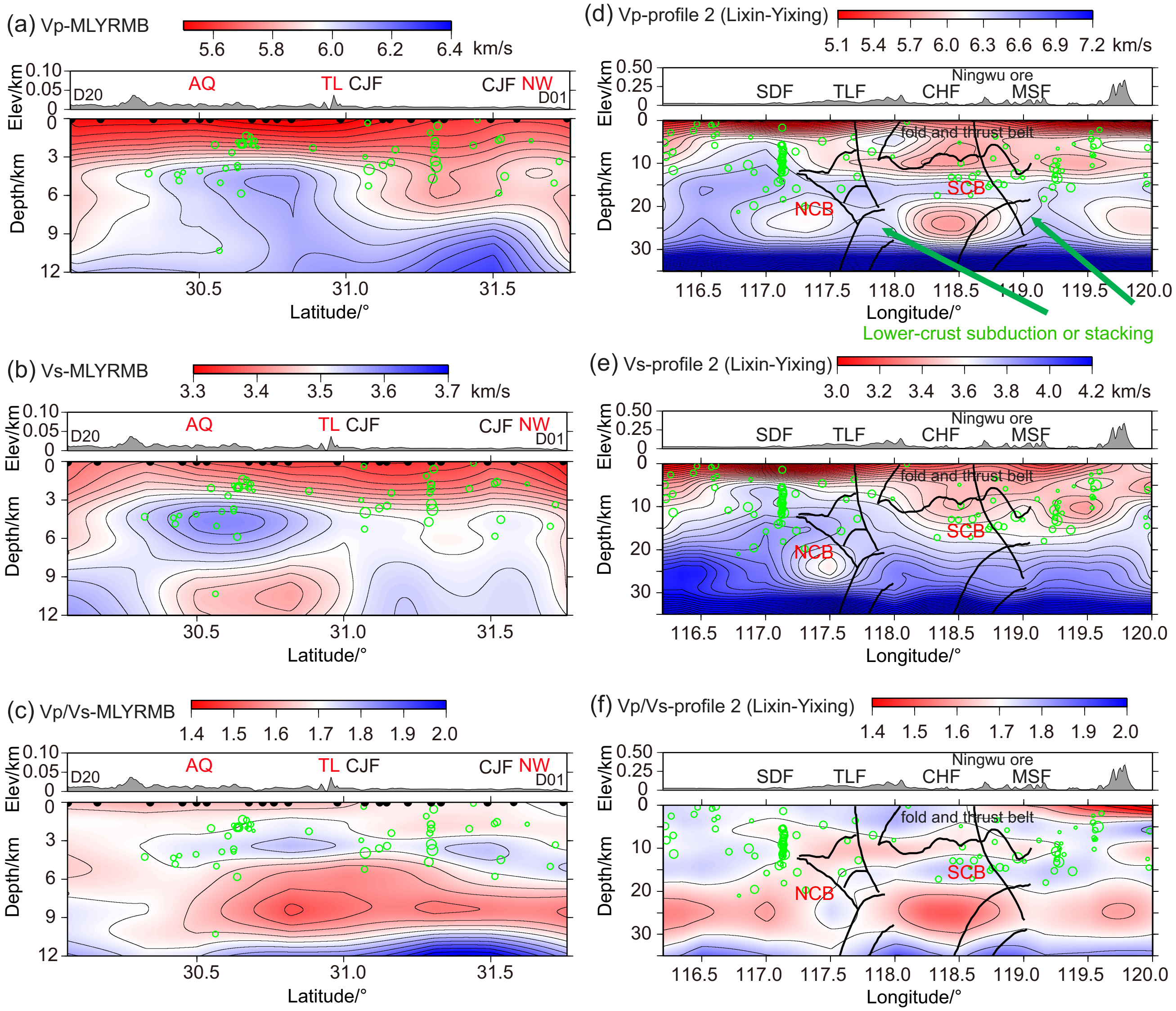

Figure 14. Vertical depth sections of the *P*-wave, *S*-wave velocity images and *Vp*/*Vs* models from the combined inversion of the active sources and the local earthquakes: (a)–(c) profile BB′ in Fig. 1 and (d)–(f) Lixin-Yixing (profile 2 in Fig. 1). Black solid lines in (d)–(f) are the schematic geodynamic model of the Middle-Lower Yangtze River Metallogenic Belt (Lyu *et al.* 2015).

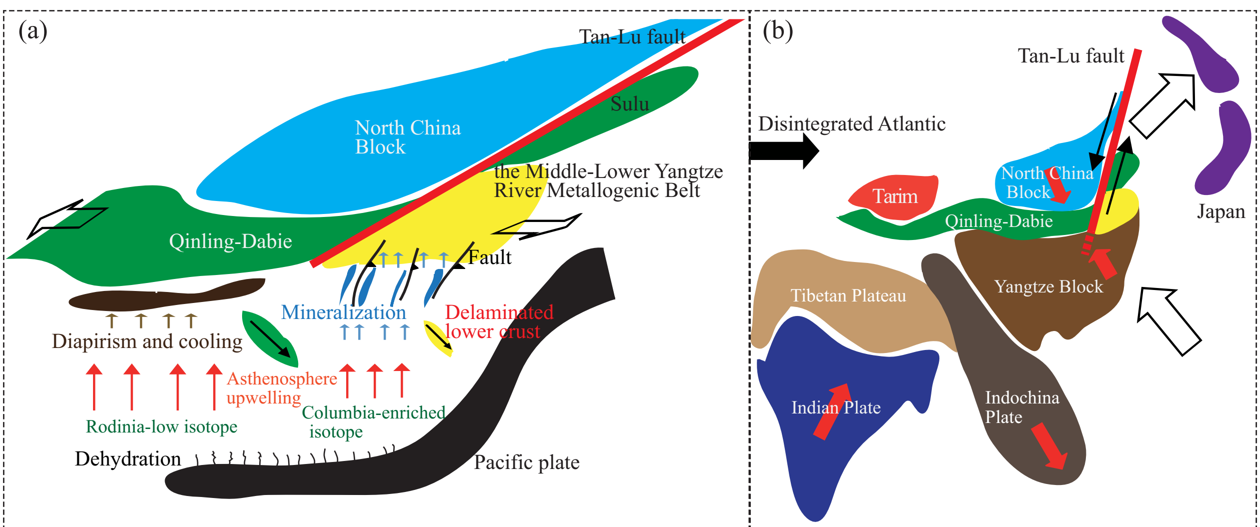

Figure 15. Cartons illustrating the geodynamic evolution of the Tan-Lu fault.

found that high-velocity anomalies exist from the uppermost mantle to a depth of at least 110 km under the eastern part of the Qingling-Dabie orogenic belt, which may represent a remnant of the subducted Yangtze block during Triassic continent–continent collision.

5.4 Velocity structures beneath the Middle-Lower Yangtze River Metallogenic Belt

To better understand the characteristics of the Middle-Lower Yangtze River Metallogenic Belt, we show two vertical depth sections (profile BB′ and profile 2 in Fig. 1) along the Yangtze River including the Tongling, Anqing and Ningwu ore deposits.

The *P*- and *S*-wave velocity images (Figs 14a and b) present similar large-scale patterns with strong deformation in the upper crust and show high velocity and high *Vp*/*Vs* (Fig. 14c) beneath the Tongling, Ningwu and Anqing ore deposits. From the surface to 5 km, there is a low-velocity anomaly beneath the Middle-Lower Yangtze River Metallogenic Belt (Figs 14a and b), corresponding to the result of Luo *et al.* (2019) and they explained the low-velocity may be related to the weak sediments in the plains and volcanic basins. In addition, a low-velocity anomaly extending to ∼9 km is observed beneath the Changjiang fault (Figs 14a and b), which corresponds to the junction zone of the Tongling, Ningwu and Luzong ore deposits.

The high- and low-velocity distributions of our imaging results beneath the Middle-Lower Yangtze River Metallogenic Belt are in accordance with the schematic geodynamic model (black solid lines in Figs 14d–f) from Lyu *et al.* (2015). Low velocities exist generally in the upper crust beneath the fold and thrust belt. Conversely, the lower crust and uppermost mantle subduction area beneath the Tan-Lu fault and the Ningwu ore district present high velocities, corresponding to the Moho uplift from receiver function result (Shi *et al.* 2013) and can be interpreted as the lower-crust subduction or stacking (Lyu *et al.* 2015).

Overall, the Tongling, Ningwu and Anqing ore deposits have high *Vp*, *Vs* and *Vp*/*Vs* in the upper crust, even in the middle and lower crust (Fig. 11), in accordance with the result of Luo *et al.* (2019). Tian *et al.* (2018) and She *et al.* (2018) proposed that the high-velocity characteristics of ore deposits are interrelated to the existence of volcanic rocks and intrusive rocks. These may be directly related to large-scale magmatism and mineralization caused by lithospheric delamination and asthenospheric upwelling (Xu *et al.* 2014; Lyu *et al.* 2015; Luo *et al.* 2019; Meng *et al.* 2019), as strongly evidenced by the Moho and LAB uplift (Shi *et al.* 2013) beneath the Ningwu ore district.

5.5 Geodynamic modelling of the evolution of the Tan-Lu fault

According to our velocity images and previous studies of other researchers (Wan *et al.* 1996; Zhao & Zheng 2009; Liang 2018; Liu *et al.* 2018; Luo *et al.* 2019; Meng *et al.* 2019), we depict in Fig. 15 the geodynamic evolution beneath the southern segment of the Tan-Lu fault.

Before the Indosinian Movement in the Mesozoic, the Yangtze block subducted beneath the North China block, bringing terrestrial sedimentary rocks and continental crust to the deep. Then these material melted and participated in the mantle cycle, transforming the deep mantle composition (Liu *et al.* 2018). During the collision between the Yangtze and the North China blocks (Fig. 15b) in the Indosinian Movement (230–208Ma), the Qinling-Dabie and Sulu orogenic belts uplifted and the Tan-Lu fault formed with 430 km of accumulated sinistral strike slip and 15–20 km cutting depth (Wan *et al.* 1996).

Because the westward subduction of the Pacific Plate beneath the Asian continent in the Early Cretaceous (Zhao *et al.* 2009), the stress state around the Tan-Lu fault changed from compression to extension (Liang 2018; Liu *et al.* 2018). The slab-released fluids caused the melting of mantle wedge material (Fig. 15a), resulting in asthenosphere upwelling. Then the thickened lower crust due to underplating was eclogitizated and hence delaminated (Fig. 15a). Following the asthenosphere material continued to uplift, the upwelling mantle materials and middle-lower crust partially melted to produce magma.

Beneath the Qinling-Dabie orogenic belt (Fig. 15a), the magma entered the overlying crust through diapirism and squeezing, and then straightly cooled in the middle crust as UHP rocks and present high-velocity structure (Zhao & Zheng 2009; Meng *et al.* 2019). Beneath the Middle-Lower Yangtze River Metallogenic Belt (Fig. 15a), magma flowed along faults and mineralized to ore deposits in a MASH (melting-assimilation-storage-homogenization) process (Lyu *et al.* 2015; Liu *et al.* 2018; Luo *et al.* 2019). The Middle-Lower Yangtze River Metallogenic Belt can form ore deposits because the magma come from the assembly and breakup of supercontinent Columbia, which contains enriched isotope. However, the magma beneath the Qinling-Dabie orogenic belt come from supercontinent Rodinia with low isotope (Zhao & Zheng 2009; Meng *et al.* 2019).

In the Cenozoic, Tan-Lu fault connected the south to north and grew into a lithospheric fault with 50–80 km cutting depth (Wan *et al.* 1996). Influenced by the southwest compression of the Yangtze block and pulling force by the cracking-drifting of the microcontinent blocks in the northeast side (Fig. 15b), the Tan-Lu fault once again experienced large-scale sinistral strike-slip activities began at 65 Ma (Liang 2018). This process was accompanied by the formation of the Cenozoic rift basins and the continuous eruption of basalt along the fault zone (Wan *et al.* 1996; Liang 2018). Influenced by the westward motion due to the back arc spreading in Pacific Plate, the Tan-Lu fault shows right-lateral strike slip since the Neogene (Zhu *et al.* 2004).

6 CONCLUSIONS

In this paper, we used the data obtained from the Anhui Airgun Experiment and local earthquakes to study the high-resolution velocity structures beneath the southern segment of the Tan-Lu fault using TOMOG3D (Zhao *et al*. 1992, 1994). The *Vp* and *Vs* crustal structures are consistent with the local geological settings, strong velocity contrasts are observed across the Tan-Lu fault zone, which is the main factor controlling local anomalies. The earthquakes are primarily clustered near faults and are spatially correlated with low-velocity zones. The high *Vp*, *Vs* and *Vp*/*Vs* beneath the Qinling-Dabie orogenic belt and the Middle-Lower Yangtze River Metallogenic Belt may relate to the lithospheric delamination and asthenospheric upwelling in the Mesozoic.

Overall, our tomographic images of the *P*- and *S*-wave velocity can help better understanding the geological issues. These results also indicate that mobile large-volume airgun sources are promising tools for 3-D crustal structure surveys and have higher resolvability in the shallow crust than local earthquakes.

ACKNOWLEDGEMENTS

We are grateful to Data Management Centre of China National Seismic Network at Institute of Geophysics (SEISDMC, doi:10.11998/SeisDmc/SN, http://www.seisdmc.ac.cn; Zheng *et al.* 2010), Geophysical Exploration Center of China Earthquake Administration, Anhui Earthquake Agency and Fujian Earthquake Agency for their data supporting. We thank Prof Dapeng Zhao for providing the TOMOG3D program (Zhao *et al*. 1992, 1994) and thoughtful comments on the manuscript. We are also grateful to the constructive comments from Huajian Yao and Yonghua Li. The Figures are produced by GMT (Wessel *et al.* 2013). This work is supported jointly by the National Natural Science Foundation of China (Grant Nos. 41674061, 41674058, 41790462 and 41790464) and Basic Research Funds from the Institute of Geophysics, China Earthquake Administration (Grant No. DQJB17T04). Thanks to reviewers and editor for their constructive comments.

REFERENCES

Aster, R.C., Borchers, B. & Thurber, C.H., 2013. *Parameter Estimation and Inverse Problems (Second Edition),* Academic Press, doi:10.1016/C2009-0-61134-X.

Bai, Z. & Wang, C., 2006. Crustal P-wave velocity structure in Lower Yangtze region: reinterpretation of Fuliji-Fengxian deep seismic sounding profile (in Chinese with English abstract), *Chinese Sci. Bull.,* **51**(21), 2534–2541.

Bai, Z., Wu, Q., Xu, T. & Wang, X., 2016. Basic features of crustal structure in the Lower Yangtze and its neighboring area of Chinese Mainland: review of deep seismic sounding research, *Earthq. Res. China,* **30**(3), 298–315.

Cai, H.-T., Hao, K.-C., Jin, X., Wang, C.-Y., Huang, B.-S. & Yen, H.-Y., 2015. A three-dimensional Vp, Vs, and Vp/Vs crustal structure in Fujian, Southeast China, from active- and passive-source experiments, *J. Asian Earth Sci.,* **111,** 517–552.

Calvert, A.J., Klemperer, S.L., Takahashi, N. & Kerr, B.C., 2008. Three-dimensional crustal structure of the Mariana island arc from seismic tomography, *J. geophys. Res.,* **113**(B1), B01406. doi:10.1029/2007JB004939.

Chen, Y., Wang, B. & Yao, H., 2017. Seismic airgun exploration of continental crust structures, *Sci. China Earth Sci.,* **60**(10), 1739–1751.

Crosson, R.S., 1976. Crustal structure modeling of earthquake data: 1. simultaneous least squares estimation of hypocenter and velocity parameters, *J. geophys. Res.,* **81**(17), 3036–3046.

Data Management Centre of China National Seismic Network, 2007. *Waveform Data of China National Seismic Network,* Institute of Geophysics, China Earthquake Administration. doi:10.11998/SeisDmc/SN, http://www.seisdmc.ac.cn.

Deng, Y., Fan, W., Zhang, Z. & Badal, J., 2013. Geophysical evidence on segmentation of the Tancheng-Lujiang fault and its implications on the lithosphere evolution in east china, *J. Asian Earth Sci.,* **78**(S1), 263–276.

Ding, W.-X., Fu, Y.-Y., Gao, Y., Liao, W.-L., He, Y.-J., Cai, Y.-J. & Shen, X.-L., 2017. Phase velocity tomography of Rayleigh in Qinling-Dabie and its adjacent areas using ambient seismic noise (in Chinese with English abstract), *Chinese J. Geophys.,* **60**(8), 2959–2968.

Dong, S., Xiang, H., Gao, R., Lyu, Q., Li, J., Zhan, S., Lu, Z. & Ma, L., 2010. Deep structure and ore formation within Lujiang-Zongyang volcanic ore concentrated area in middle to lower reaches of Yangtze River (in Chinese with English abstract), *Acta Petrol. Sin.,* **26**(9), 2529–2542.

Eberhart-Phillips, D., 1986. Three-dimensional velocity structure in northern California coast ranges from inversion of local earthquake arrival times, *Bull. seism. Soc. Am.,* **76**(8864), 1025–1052.

Evangelidis, C.P., Minshull, T.A. & Henstock, T.J., 2004. Three-dimensional crustal structure of ascension island from active source seismic tomography, *Geophys. J. Int.,* **159**(1), 311–325.

García-Yeguas, A., Koulakov, I., Ibáñez, J.M. & Rietbrock, A., 2012. High resolution 3D P wave velocity structure beneath Tenerife Island (Canary Islands, Spain) based on tomographic inversion of active-source data, *J. geophys. Res.,* **117,** B09309. doi:10.1029/2011JB008970.

Ge, R.-F., Zhang, Q.-L., Xie, G.-A., Xu, S.-Y., Wang, X.-Y. & Chen, J., 2009. Seismic activity and stress state of the northern Tanlu fault zone and its adjacent areas (in Chinese with English abstract), *Seismol. Geol.,* **31**(1), 141–154.

Godfrey, N.J., Christensen, N.I. & Okaya, D.A., 2002. The effect of crustal anisotropy on reflector depth and velocity determination from wide-angle seismic data: a synthetic example based on south island, new Zealand, *Tectonophysics,* **355**(1), 145–161.

Gu, Q.-P., Ding, Z.-F., Kang, Q.-Q. & Zhao, Q.-G., 2016. Pn wave velocity and anisotropy in the middle-southern segment of the Tan-Lu fault zone and adjacent region (in Chinese with English abstract), *Chinese J. Geophys.,* **59**(2), 504–515.

Guo, Y., Xu, J., Lin, C., Jin, X., Yao, H., Yang, H. & Cai, H., 2019. Experiments on exploration of shallow fine structures and the construction of the 1-D velocity model in the Pingtan Island, Fujian, *Earthq. Res. China,* **33**(2), 265–257.

Hao, Y., Magnani, M.B., McIntosh, K., Waldron, B. & Guo, L., 2013. Quaternary deformation along the Meeman-Shelby Fault near Memphis, Tennessee, imaged by high-resolution marine and land seismic reflection profiles, *Tectonics,* **32,** 501–515.

He, R., Shang, X., Yu, C., Zhang, H. & Van der Hilst, R.D., 2014. A unified map of Moho depth and Vp/Vs ratio of continental china by receiver function analysis, *Geophys. J. Int.,* **199**(3), 1910–1918.

Hou, Z.-Q., Pan, X.-F., Yang, Z.-M. & Qu, X.-M., 2007. Porphyry Cu-(Mo-Au) deposits no related to oceanic-slab subduction: examples from Chinese porphyry deposits in continental settings (in Chinese with English abstract), *Geoscience,* **21**(2), 332–351.

Huang, Y., Li, Q.-H., Zhang, Y.-S., Sun, Y.-J., Bi, X.-M., Jin, S.-M. & Wang, J., 2011. Crustal velocity structure beneath the Shandong-Jiagsu-Anhui segment of the Tancheng-Lujiang Fault Zone and adjacent areas (in Chinese with English abstract), *Chinese J. Geophys.,* **54**(10), 2549–2559.

Jiang, G., Zhang, G., Lyu, Q., Shi, D. & Xu, Y., 2013. 3-D velocity model beneath the middle–lower Yangtze river and its implication to the deep geodynamics, *Tectonophysics,* **606**(142), 36–47.

Jiang, S., Wang, B., Zhang, Y. & Chen, Y., 2017. The influence of noise on the stacking effect of airgun signal and the automatic data screening method (in Chinese with English abstract), *J. Seismol. Res.,* **40**(4), 534–542.

Kissling, E., Ellsworth, W.L., Eberhart-Phillips, D. & Kradolfer, U., 1994. Initial reference models in local earthquake tomography, *J. geophys. Res.,* **99**(B10), 19 635–19 646.

Kissling, E., 1995. *Velest User's Guide. Internal Report 26,* Institute of Geophysics, ETH Zurich.

Laske, G., Masters, G., Ma, Z. & Pasyanos, M., 2013. Update on CRUST1.0–a 1-degree Global Model of Earth's Crust, *Geophys. Res. Abstracts,* **15,** Abstract EGU2013-2658. doi:10.6092/1970-9870/128.

Li, S.-G., 2001. Infrastructure of Mesozoic magmatic rocks and copper-iron metallogenic belt in the middle and lower Yangtze River reaches (in Chinese with English abstract), *Geol. Anhui,* **11**(2), 118–122.

Li, Y., Dong, S., Zhang, Z., Gao, R. & Lu, D., 2002. Poisson's ratio structure of the crust and UHP metamorphic zone in the Dabie orogenic belt (in Chinese with English abstract), *Geology Review,* **48**(1), 15–23.

Li, Y., Gao, M. & Wu, Q., 2014. Crustal thickness map of the chinese mainland from teleseismic receiver functions, *Tectonophysics,* **611,** 51–60.

Li, X.-H., Li, Z.-X., Li, W.-X., Wang, X.-C. & Gao, Y.-Y., 2013. Revisiting the "C-type adakites" of the Lower Yangtze River Belt, central eastern China: in-situ zircon Hf-O isotope and geochemical constraints, *Chem. Geol.,* **345**(1), 1–15.

Liang, G., 2018. Discussion on several key problems of the Tanlu Fault (in Chinese with English abstract), *Gold Sci. Technol.,* **26**(5), 543–558.

Ling, M.-X., Wang, F.-Y., Ding, -X., Hu, Y.-H., Zhou, J.-B., Zartman, R.E., Yang, X.-Y. & Sun, W., 2009. Cretaceous ridge subduction along the lower Yangtze River Belt, Eastern China, *Econ. Geol.,* **104**(2), 303–321.

Liu, B.-J., Feng, S.-Y., Ji, J.-F., Shi, J.-H., Tan, Y.-L. & Li, Y.-Q., 2015. Fine lithosphere structure beneath the middle-southern segment of the Tan-Lu fault zone (in Chinese with English abstract), *Chinese J. Geophys.,* **58**(5), 1610–1621.

Liu, D., Xia, R., Liu, Z., Shen, X., Li, M. & Yan, S., 2006. Characteristics of recent seismicity and stress fields in Anhui sector of the Tan-Lu fault zone (in Chinese with English abstract), *Chinese J. Geol.,* **42**(2), 278–290.

Liu, X., Yan, J., Wang, A, Li, Q. & Zhang, Y., 2016. Geochronological study on Mesozoic magmatic rocks in Yuexi area, Dabie Orogen (in Chinese with English abstract), *Geol. Rev.,* **62**(4), 897–914.

Liu, Z., Yang, X., Liu, C., Huang, D., Zhou, W., Teng, X., Liang, E. & Dai, T., 2018. Genesis of Early Cretaceous porphyrite-type iron deposits and related sub-volcanic rocks in the Ningwu Volcanic Basin, Middle-Lower Yangtze Metallogenic Belt, Southeast China, *Int. Geol. Rev.,* **60**(11–14), 1507–1528.

Long, L.T. & Zelt, K.H., 1991. A local weakening of the brittle-ductile transition can explain some intraplate seismic zones, *Tectonophysics,* **186**(1–2), 175–192.

Luo, Y., Xu, Y. & Yang, Y., 2012. Crustal structure beneath the Dabie orogenic belt from ambient noise tomography, *Earth Planet. Sci. Lett.,* **313–314,** 12–22.

Luo, Z.-L., Li, J.-M., Li, X.-J., Liu, S.-G., Zhao, X.-K. & Sun, W., 2005. Discussion on the formation, evolution and problems of the Tancheng-Lujiang fault zone (in Chinese with English abstract), *J. Jilin Univ. (Earth Science Edition),* **35**(6), 699–706.

Luo, S., Yao, H., Li, Q., Wang, W., Wan, K., Meng, Y. & Liu, B., 2019. High-resolution 3D crustal S-wave velocity structure of the middle-lower Yangtze River Metallogenic Belt and implications for its deep geodynamic setting, *Sci. China Earth Sci.,* **62**(9), 1361–1378.

Lyu, Q. *et al.*, 2003. Deep seismic reflection profiling revealing the complex crustal structure of the Tongling ore district (in Chinese with English abstract), *Sci. China, Ser., D,* **33**(5), 442–449.

Lyu, Q., Hou, Z., Yang, Z. & Shi, D., 2005. Underplating in the middle-lower Yangtze Valley and model of geodynamic evolution: constraints from geophysical data, *Sci. China, Ser., D,* **48**(7), 985–999.

Lyu, Q., Shi, D., Liu, Z., Zhang, Y., Dong, S. & Zhao, J., 2015. Crustal structure and geodynamics of the middle and lower reaches of Yangtze metallogenic belt and neighboring areas: insights from deep seismic reflection p-rofiling, *J. Asian Earth Sci.,* **114,** 704–716.

Matrullo, E., Matteis, R.D., Satriano, C., Amoroso, O. & Zollo, A., 2013. An improved 1-D seismic velocity model for seismological studies in the Campania-Lucania region (Southern Italy), *Geophys. J. Int.,* **195**(1), 460–473.

Meng, Y., Yao, H., Wang, X., Li, L., Feng, J., Hong, D. & Wang, X., 2019. Crustal velocity structure and deformation features in the central-southern segment of Tanlu fault zone and its adjacent area from ambient noise tomography (in Chinese with English abstract), *Chinese J. Geophys.,* **62**(7), 2490–2509.

Ouyang, L.-B. *et al.*, 2015. Crustal shear wave velocity structure and radial anisotropy beneath the middle-lower Yangtze River metallogenic belt and surrounding areas from seismic ambient noise tomography (in Chinese with English abstract), *Chinese J. Geophys.,* **58**(12), 4388–4402.

Paulatto, M., Annen, C., Henstock, T.J., Kiddle, E., Minshull, T.A., Sparks, R.S.J. & Voight, B., 2012, Magma chamber properties from integrated seismic tomography and thermal modeling at Montserrat, *Geochem. Geophys. Geosyst.,* **13,** Q01014. doi:10.1029/2011GC003892.

Qiu, X., Chen, Y., Zhu, R., Xu, H., Shi, X., Ye, C., Zhao, M. & Xia, S., 2007. The application of large volume airgun sources to the onshore-offshore seismic surveys: implication of the experimental results in northern South China Sea (in Chinese with English abstract), *Chinese Sci. Bull.,* **52**(4), 463–469.

Ryberg, T., Hole, J.A., Fuis, G.S., Rymer, M.J., Bleibinhaus, F., Stromeyer, D. & Bauer, K., 2012. Tomographic Vp and Vs structure of the California central coast ranges, in the vicinity of Safod, from controlled-source seismic data, *Geophys. J. Int.,* **190**(3), 1341–1360.

Shalev, E. *et al.*, 2010. Three-dimensional seismic velocity tomography of Montserrat from the Sea-Calipso offshore/onshore experiment, *Geophys. Res. Lett.,* **37,** L00E17. doi:10.1029/2010GL042498.

She, Y., Yao, Y., Zhai, Q., Wang, F. & Tian, X., 2018. Shallow crustal structure of the middle-lower Yangtze River Region in Eastern China from surface-wave tomography of a large volume airgun-shot experiment, *Seismol. Res. Lett.,* **89**(3), 1003–1013.

Shi, W., Zhang, Y. & Dong, S., 2003. Quaternary activity and segmentation behavior of the middle portion of the Tan-Lu fault zone (in Chinese with English abstract), *Acta Geosci. Sin*. **24**(1), 11–18.

Shi, D., Lyu, Q., Xu, W., Yan, J., Zhao, J., Dong, S. & Chang, Y., 2013. Crustal structure beneath the middle–lower Yangtze metallogenic belt in East China: constraints from passive source seismic experiment on the Mesozoic intra-continental mineralization. *Tectonophysics,* **606,** 48–59.

Syracuse, E.M., Zhang, H. & Maceira, M., 2017. Joint inversion of seismic and gravity data for imaging seismic velocity structure of the crust and upper mantle beneath Utah, United States, *Tectonophysics,* **718,** 105–117.

Thurber, C.H., 1983. Earthquake locations and three-dimensional crustal structure in the Coyote Lake Area, central California, *J. geophys. Res.,* **88**(B10), 8226–8236.

Tian, X. *et al.*, 2018. 3D seismic refraction travel-time tomography beneath the middle-lower Yangtze River region, *Seismol. Res. Lett.,* **89**(3), 992–1002.

Vaage, S., Haugland, K. & Utheim, T., 1983. Signatures from single airguns, *Geophys. Prospect.,* **31**(1), 87–97.

Wan, T., Zhu, H., Zhao, L., Lin, J., Cheng, J. & Chen, J., 1996. Formation and evolution of the Tancheng-Lujiag fault zone: a review (in Chinese with English abstract), *Geoscience,* **10**(2), 159–168.

Wan, G., Tang, L., Jin, W. & Yu, Y., 2009. Progresses and problems in the study of Tancheng-Luiang fault zone (in Chinese with English abstract), *Geol. Rev.,* **55**(2), 251–259.

Wang, B. *et al.*, 2018. Seismic signature of an untuned large-volume airgun array fired in a water reservoir, *Seismol. Res. Lett.,* **89**(3), 983–991.

Wang, B., Yang, W., Wang, W., Yang, J., Li, X. & Ye, B., 2020. Diurnal and semidiurnal P- and S-wave velocity changes measured using an airgun source, *J. geophys. Res.,* doi:10.1029/2019JB018218.

Wang, C.-Y., Zeng, R.-S., Mooney, W.D. & Hacker, B.R., 2000. A crustal model of the ultrahigh-pressure Dabie Shan orogenic belt, China, derived from deep seismic refraction profiling, *J. geophys. Res.,* **105**(B5), 10857–10869.

Weng, S., Chen, H., Zhou, X. & Cui, Z., 1990. Deep seismic probing of continental crust in the lower Yangtze region, eastern China, *Tectonophysics,* **173**(1–4), 297–305.

Wessel, P., Smith, W.H.F., Scharroo, R., Luis, J. & Wobbe, F., 2013. Generic mapping tools: improved version released, *EOS, Trans. Am. Geophys. Un.,* **94**(45), 409–410.

Wu, Z.-H., Zhou, C.-J., Tan, C.-X., Sun, Y.-J. & Ma, X.-X., 2016. The active tectonics and regional crustal stability features in the area of Yangtze River Economic Belt (in Chinese with English abstract), *J. Geomech.,* **22**(3), 379–411.

Xu, J., Cai, H., Jin, X., Wang, S., Xia, J. & Li, P., 2016. Signal detection of large volume airgun source excitation in the fixed field of the Yangtze River, *Earthq. Res. China,* **30**(3), 418–429.

Xu, J. & Zhu, G., 1995. Discussion on tectonic model for the Tanlu fault zone, eastern China (in Chinese with English abstract), *J. Geol. Miner Res. N. China,* **10**(2), 121–134.

Xu, P.-F., Liu, F.-T., Wang, Q.-C., Cong, B.-L., Chen, H. & Sun, R.-M., 2000. Seismic tomography beneath the Dabie-Sulu collision orogen—3-D velocity structures of lithosphere (in Chinese with English abstract), *Chinese J. Geophys.,* **43**(3), 377–385.

Xu, P., Liu, F., Wang, Q., Cong, B. & Chen, H., 2001. Slab-like high velocity anomaly in the uppermost mantle beneath the Dabie-Sulu Orogen, *Geophys. Res. Lett.,* **28**(9), 1847–1850.

Xu, T., Zhang, Z., Tian, X., Liu, B., Bai, Z., Lyu, Q. & Teng, J., 2014. Crustal structure beneath the Middle-Lower Yangtze metallogenic belt and its surrounding area: constraints from active source seismic experiment along the Lixin to Yixing profile in East China (in Chinese with English abstract), *Acta Petrol. Sin.,* **30**(4), 918–930.

Xu, X. & Gao, S., 2015. The structure and formation of the Cenozoic fault basin in the Lower Yangtze region (in Chinese with English abstract), *Earth Sci. Front.*. **22**(6), 148–166.

Yang, W., 2002. Geophysical profiling across the Sulu ultra-high-pressure metamorphic belt, eastern China, *Tectonophysics*. **354**(3), 277–288.

Yao, Y. & Fang, Z., 1981. Brief report on the "symposium on Tancheng-Lujiang fault zone" (in Chinese with English abstract), *Seismol. Geol.,* **3**(2), 69–78.

Yao, D., Gong, X., Shen, X., Wu, W., Zheng, H., Chen, A. & Yang, Y., 2014. Research progress of prehistoric earthquake of Anhui Province and its neighborhood (in Chinese with English abstract), *Chinese J. Geol.,* **49**(2), 368–377.

Yin, A. & Nie, S., 1993. An indentation model for the North and South China collision and the development of the Tan-Lu and Honam fault systems, eastern Asia, *Tectonics,* **12**(4), 801–813.

Zandomeneghi, D., Barclay, A., Almendros, J., Ibañez Godoy, J.M., Wilcock, W.S.D. & Ben-Zvi, T., 2009. Crustal structure of deception Island volcano from P wave seismic tomography: tectonic and volcanic implications, *J. geophys. Res.,* **114,** B06310. doi:10.1029/2008JB006119.

Zhang, H., Maceira, M., Roux, P. & Thurber, C., 2014. Joint inversion of body-wave arrival times and surface-wave dispersion for three-dimensional seismic structure around SAFOD, *Pure appl. Geophys.,* **171**(11), 3013–3022.

Zhang, J., Shen, X., Wang, X. & Shen, Y., 2005. Discussion on deep tectonic backgrounds of moderate-strong earthquake in Anhui and its neighboring region by using results of seismic tomography (in Chinese with English abstract), *Earthq. Res. China,* **21**(3), 350–359.

Zhang, Y., Wang, B., Wang, W. & Xu, Y., 2016. Preliminary results of tomography from permanent stations in the Anhui Airgun Experiment, *Earthq. Res. China,* **30**(3), 405–417.

Zhao, D., Hasegawa, A. & Horiuchi, S., 1992. Tomographic imaging of P and S wave velocity structure beneath northeastern Japan, *J. geophys. Res.,* **97**(B13), 19 909–19 928.

Zhao, D., Hasegawa, A. & Kanamori, H., 1994. Deep structure of Japan subduction zone as derived from local, regional, and teleseismic events, *J. geophys. Res.,* **99**(B11), 22 313–22 329.

Zhao, D., Todo, S. & Lei, J., 2005. Local earthquake reflection tomography of the Landers aftershock area, *Earth Planet. Sci. Lett.,* **235**(3–4), 623–631.

Zhao, D., Tian, Y., Lei, J., Liu, L. & Zheng, S., 2009. Seismic image and origin of the Changbai intraplate volcano in East Asia: role of big mantle wedge above the stagnant Pacific slab. *Phys. Earth planet. Inter.,* **173,** 197–206.

Zhao, Z. & Zheng, Y., 2009. Remelting of subducted continental lithosphere: Petrogenesis of Mesozoic magmatic rocks in the Dabie-Sulu orogenic belt, *Sci. China, Ser., D,* **52**(9), 1295–1318.

Zheng, X.-F., Yao, Z.-X., Liang, J.-H. & Zheng, J., 2010. The role played and opportunities provided by IGP DMC of China National Seismic Network in Wenchuan earthquake disaster relief and researches, *Bull. seism. Soc. Am.,* **100**(5B), 2866–2872.

Zheng, Y. & Teng, J.-W., 1989. The structure of the crust and upper mantle in the Suixian-Maanshan zone and some characteristics of the south part of the Tan-Lu tectonic belt (in Chinese with English abstract), *Chinese J. Geophys.,* **32**(6), 648–659.

Zhu, G., Wang, D., Liu, G., Niu, M. & Song, C., 2004. Evolution of the Tan-Lu fault zone and its responses to plate movement in west Pacific basin (in Chinese with English abstract), *Chinese J. Geol.,* **39**(1), 36–49.

Zollo, A., Judenherc, S., Auger, E., D'Auria, L., Virieux, J. & Gapuano, P., 2003. Evidence for the buried rim of Campi Flegrei caldera from 3-D active seismic imaging, *Geophys. Res. Lett.,* **30**(19). doi:10.1029/2003GL018173.